Markou, Anastasia; St-Pierre, Luc

A novel parameter to tailor the properties of prismatic lattice materials

Published in:
International Journal of Mechanical Sciences

DOI:
10.1016/j.ijmecsci.2022.107079

Published: 01/04/2022

Document Version
Publisher's PDF, also known as Version of record

International Journal of Mechanical Sciences 219 (2022) 107079

Contents lists available at ScienceDirect

International Journal of Mechanical Sciences

journal homepage: www.elsevier.com/locate/ijmecsci

A novel parameter to tailor the properties of prismatic lattice materials

Anastasia Markou, Luc St-Pierre *

Aalto University, Department of Mechanical Engineering, PO box 14100, FI-00076 Aalto, Finland

ARTICLE INFO

Keywords:
Lattice materials
Cellular solids
Honeycombs
Hexagonal lattice
Triangular lattice

ABSTRACT

Lattice materials are extremely efficient in combining high stiffness and strength at low densities. Their architecture is a periodic assembly of bars, which, in most cases, all have the same length and cross-section. This is, however, suboptimal since the level of stress is not the same in all bars. To take these variations into account, we propose to design prismatic lattices with two different bar thicknesses. The ratio of these two thicknesses introduces a new parameter in the design of lattices. Analytical expressions are developed to capture the effect of this new parameter on the elastic modulus, failure mode and compressive strength of hexagonal and triangular lattices. This analytical work is then validated by finite element simulations and experiments performed on polymer lattices fabricated by additive manufacturing. This new parameter offers two advantages in the design of prismatic lattices. First, the thickness ratio can be used to vary the properties of a lattice without changing its relative density. Second, it allows to stiffen and strengthen the lattice along a specific loading direction and therefore, controls the degree of anisotropy. This work opens new possibilities to tailor the mechanical properties of prismatic lattices, and facilitates the creation of new materials by design.

1. Introduction

Lattice materials can be designed to have precise, and often unique, mechanical properties [1,2]. Their properties are a function of three parameters: (i) the parent material from which the lattice is made of, (ii) its topology and (iii) its relative density $\bar{\rho}$ (which represents the volume fraction of material) [3]. For example, the elastic modulus of a lattice can be expressed as [4]:

$$E = B\bar{\rho}^{b}E_{s}, \quad (1)$$

where E_s is the Young's modulus of the parent material, whereas B and b are two constants dependent upon the topology of the lattice. Optimising the architecture to maximise the elastic modulus has been the subject several investigations, and a number of highly efficient isotropic topologies have been identified recently [5–7].

Fabricating these optimised topologies has become significantly easier with the recent and rapid development of additive manufacturing [8,9]. On one hand, this technology facilitated the production of existing concepts, such as truss lattices [10–14]; shell lattices [15,16]; and hierarchical topologies [17–22]. On the other hand, additive manufacturing and rapid prototyping technologies opened new opportunities to customise the design of lattices and enhance their properties. One example is the development of ultralight micro-lattices that are strengthen by material size effects [23–27]. Other examples include lattices with tapered beams [28–30], or an origami architecture [31] to increase their energy absorption; topologies combining two dissimilar materials to achieve high strength and high compressive strains [32]; and architectures with wavy struts to enhance their tensile fracture strain [33,34].

Additive manufacturing also offers the possibility to optimise the properties of lattices by changing the distribution of material. Previous studies on this topic can be categorised in two groups depending if the optimisation is done at (i) the structural length-scale or (ii) the unit cell level. In the former group, the properties of a lattice structure are optimised for specific loading conditions by spatially varying the relative density [35–39]. These are commonly referred to as graded architectures. In the latter group, computational topology optimisation is used to design the unit cell of the lattice, based on a set of constraints and objective functions [40–43]. While these optimisation approaches can lead to highly efficient topologies, they are computationally expensive and often restricted to elastic properties only. These limitations highlight the need to investigate analytically the effect of mass distribution in lattices, and this is the subject of this study.

In this work, we propose to tailor the properties of prismatic lattices by introducing two different bar thicknesses, t_1 and t_2, as shown in Fig. 1. For most loading cases, these two bars are carrying different loads and therefore, optimising their thickness accordingly has the potential to increase performances. This geometrical change introduces a new design parameter, the thickness ratio $\bar{t} = t_1/t_2$. We will show

* Corresponding author.
E-mail address: luc.st-pierre@aalto.fi (L. St-Pierre).

https://doi.org/10.1016/j.ijmecsci.2022.107079
Received 20 August 2021; Received in revised form 18 December 2021; Accepted 10 January 2022
Available online 22 January 2022

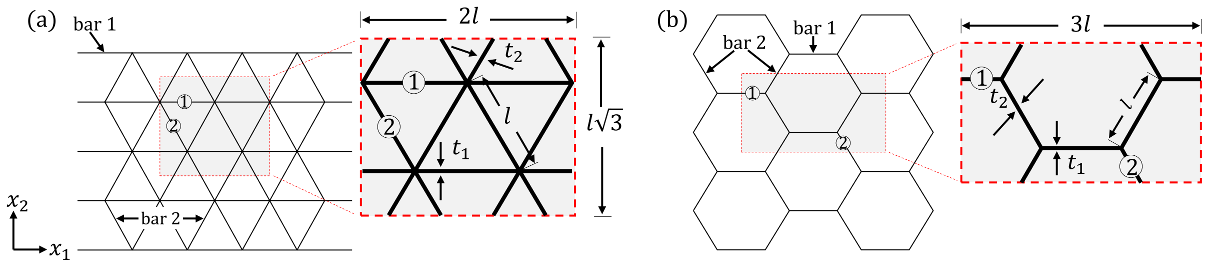

Fig. 1. Geometry of (a) triangular and (b) hexagonal lattices, where the horizontal bars, numbered 1, have a thickness t_1 and the diagonal bars, numbered 2, have a thickness t_2. The periodic unit cells used in finite element simulations are delimited by the red dashed lines.

below that $\bar{t}$ has a pronounced effect on the properties: it transforms the constant B in Eq. (1) into a function of $\bar{t}$, and this offers an opportunity to modify the properties without changing the relative density $\bar{\rho}$ of the lattice. The objective of the paper is to quantify the effect of $\bar{t}$ on the elastic modulus, compressive strength and failure modes of prismatic lattices. Our investigation focuses on hexagonal and triangular lattices since they have strikingly different behaviours: the former is bending-dominated whereas the latter is stretching-dominated.

The in-plane properties of triangular and hexagonal lattices with $\bar{t} = 1$ have been investigated both analytically and experimentally [44–46]. Hexagonal lattices with $\bar{t} = 2$ have also been the subject of many investigations [47–54]. These are expanded honeycombs, fabricated by gluing and pulling apart strips of materials, and therefore, their different bar thicknesses are simply a consequence of the manufacturing route. Nonetheless, the bar thickness has been considered as a design parameter in a number of studies. For example, hexagonal lattices with cell walls that vary in thickness along their length (thicker at the nodes than in the middle) can be stiffer and stronger than their uniform counterparts [55–58]. Others, have design honeycombs with a gradient in bar thickness to increase the transverse shear modulus [59] or, in most cases, the energy absorption capacity [60–64]. Note that in these graded honeycombs, the bar thickness is varied at different locations inside a structure (thereby modifying *structural* properties), which is different from the approach proposed here where the distribution of material is changed within the unit cell (tuning its *material* properties). Another approach to improve the properties of honeycombs has been to completely re-design their geometry, see the review of Qi et al. [65]. This, however, produces stepwise changes in properties, whereas the thickness ratio $\bar{t}$ proposed in this study enables to vary properties in a continuous manner.

This paper is structured as follows. Analytical expressions are developed in Section 2 to capture the effect of $\bar{t}$ on the mechanical properties of hexagonal and triangular lattices. These analytical results are presented in Section 3 and then validated using finite element simulations in Section 4. The study is complemented by experiments performed on samples manufactured by additive manufacturing, and these are presented in Section 5. In these experiments, $\bar{t}$ is varied by changing both t_1 and t_2 while keeping the relative density fixed. Finally, the main advantages of $\bar{t}$ are discussed in Section 6.

2. Analytical modelling

In this section, analytical expressions are derived for the elastic modulus and strength of prismatic lattices with different bar thicknesses, see Fig. 1. Triangular and hexagonal topologies are considered in turn, and equations are derived for uniaxial compression in x_1 and x_2 directions. Both lattices are assumed to be made from a linear elastic, perfectly plastic material, characterised by a Young's modulus E_s and a yield strength σ_{ys}. The cell walls of the stretching-dominated triangular lattice are considered to behave as pin-jointed trusses, whereas those of the bending-dominated hexagonal topology are modelled as Euler–Bernoulli beams. These assumptions generally acceptable provided that lattices have a relative density $\bar{\rho} \leq 0.3$ [4] and that the cell walls of the hexagonal lattice are sufficiently slender (t_1/l and t_2/l are less than 0.2) to neglect axial and shear deformations [44].

2.1. Triangular lattice

Consider the triangular lattice shown in Fig. 1a, where all bars have a length l, but not the same thickness. The horizontal bars have a thickness t_1, whereas the diagonal struts have a thickness t_2. Therefore, the relative density of the triangular lattice is given by:

$$\bar{\rho} = \frac{2\sqrt{3}}{3}\frac{(t_1 + 2t_2)}{l}. \tag{2}$$

2.1.1. Loading in x_1 direction

First, consider the triangular lattice loaded in the x_1 direction by a uniform compressive stress σ_1. The triangular lattice is stretching-dominated, and the axial forces in bars 1 and 2 are given by [45]:

$$T_1 = -\frac{\sqrt{3}}{2}\sigma_1 bl \quad \text{and} \quad T_2 = 0, \tag{3}$$

respectively, where b is the out-of-plane dimension, and the negative sign indicates a compressive force. We emphasise here that the axial forces T_1 and T_2 are independent of the bar thickness. Since only bar 1 is carrying load, the nominal compressive strain of the lattice is given by:

$$\epsilon_1 = \frac{\sqrt{3}l\sigma_1}{2t_1 E_s}, \tag{4}$$

where E_s is the Young's modulus of the parent material. The elastic modulus of the lattice in the x_1 direction is $E_1 = \sigma_1/\epsilon_1$, which gives:

$$E_1 = \left[\frac{\bar{t}}{\bar{t}+2}\right]\bar{\rho}E_s, \tag{5}$$

where the thickness ratio $\bar{t} = t_1/t_2$.

Next, we turn our attention to the compressive strength of the triangular lattice. Two collapse mechanisms are possible: (i) elastic buckling and (ii) yielding. Elastic buckling will occur when the compressive load in a bar reaches the Euler buckling load [66]:

$$T_{cr} = \frac{n^2\pi^2 E_s I}{l^2}, \tag{6}$$

where I is the second moment of area and n is the end constraint factor ($n = 1$ for pinned joints, whereas $n = 2$ when both ends are fixed). When compressed in the x_1 direction, only bar 1 is loaded in compression (see Eq. (3)), therefore setting $T_1 = T_{cr}$ gives us the elastic buckling strength:

$$\sigma_{1,el}^{[t_1]} = \frac{n^2\pi^2}{16}\left[\frac{\bar{t}}{\bar{t}+2}\right]^3\bar{\rho}^3 E_s, \tag{7}$$

where the subscript el and the superscript $[t_1]$ are used to indicate that bar 1 is buckling elastically. It is important to mention that the end constraint factor n varies with $\bar{t}$. It is possible to show analytically that n decreases from 2 to 1 as $\bar{t}$ increases from 0 to 5. This lengthy analysis relies on beam–column theory [67,68] and is provided in Appendix A.1.

The collapse mode is anticipated to change from elastic buckling to yielding as the relative density is increased. The yield strength of the lattice is obtained by setting $T_1 = bt_1\sigma_{ys}$, which gives:

$$\sigma_{1,pl}^{[t_1]} = \left[\frac{\bar{t}}{\bar{t}+2}\right]\bar{\rho}\sigma_{ys}. \tag{8}$$

Above, the subscript pl and the superscript $[t_1]$ are used to indicate that yielding occurs in bar 1. Finally, the lattice will collapse in the mode associated with the lowest stress, and therefore, its compressive strength is given by:

$$\sigma_1 = \min\left(\sigma_{1,el}^{[t_1]}, \sigma_{1,pl}^{[t_1]}\right). \tag{9}$$

2.1.2. Loading in x_2 direction

Consider the triangular lattice loaded in the x_2 direction by uniform compressive stress σ_2. For this loading scenario, the axial forces in bars 1 and 2 are [45]:

$$T_1 = \frac{\sqrt{3}}{6}\sigma_2 bl \quad \text{and} \quad T_2 = -\frac{\sqrt{3}}{3}\sigma_2 bl, \tag{10}$$

respectively. The nominal compressive strain ϵ_2 can be obtained by equating the internal strain energy to the work done by the external stress σ_2. For the unit cell in Fig. 1a, the internal strain energy is:

$$U = \frac{l}{E_s b}\left[\frac{4T_1^2}{t_1} + \frac{8T_2^2}{t_2}\right] = \frac{(8t_1+t_2)bl^3\sigma_2^2}{3t_1t_2E_s}, \tag{11}$$

whereas the work done by the external stress is $W = 2\sqrt{3}bl^2\sigma_2\epsilon_2$. Setting $U = W$ and solving for ϵ_2 returns:

$$\epsilon_2 = \frac{(8t_1+t_2)l\sigma_2}{6\sqrt{3}t_1t_2E_s}. \tag{12}$$

The elastic modulus in the x_2 direction is simply $E_2 = \sigma_2/\epsilon_2$, and this yields:

$$E_2 = \frac{9\bar{t}}{(8\bar{t}+1)(\bar{t}+2)}\bar{\rho}E_s. \tag{13}$$

The compressive strength of the triangular lattice in the x_2 direction is controlled by either elastic buckling or yielding. Elastic buckling will occur when $T_2 = T_{cr}$, which yields:

$$\sigma_{2,el}^{[t_2]} = \frac{3n^2\pi^2}{32}\left[\frac{1}{\bar{t}+2}\right]^3\bar{\rho}^3E_s. \tag{14}$$

Again, the end constraint factor n varies with $\bar{t}$ and its value is provided in Appendix A.1. Otherwise, yielding can occur in bar 1 or 2 since both struts are carrying load, see Eq. (10). Yielding in bar 1 will occur when $T_1 = bt_1\sigma_{ys}$, whereas bar 2 will yield when $T_2 = bt_2\sigma_{ys}$. This gives us:

$$\sigma_{2,pl}^{[t_1]} = 3\left[\frac{\bar{t}}{\bar{t}+2}\right]\bar{\rho}\sigma_{ys} \quad \text{and} \tag{15}$$

$$\sigma_{2,pl}^{[t_2]} = \frac{3}{2}\left[\frac{1}{\bar{t}+2}\right]\bar{\rho}\sigma_{ys}. \tag{16}$$

Finally, the compressive strength σ_2 of the triangular lattice is governed by the collapse mode which occurs at the lowest stress and this can be expressed as:

$$\sigma_2 = \min\left(\sigma_{2,el}^{[t_2]}, \sigma_{2,pl}^{[t_1]}, \sigma_{2,pl}^{[t_2]}\right). \tag{17}$$

2.2. Hexagonal lattice

The hexagonal lattice is shown in Fig. 1b and its relative density is given by:

$$\bar{\rho} = \frac{2}{3\sqrt{3}}\frac{(t_1+2t_2)}{l}. \tag{18}$$

2.2.1. Loading in x_1 direction

Consider the hexagonal lattice loaded in the x_1 direction by a uniform compressive stress σ_1. If the axial deformation of bar 1 is neglected, the hexagonal lattice deforms by bending bar 2, see Fig. 1b. Based on Gibson and Ashby [44], the nominal compressive strain is:

$$\epsilon_1 = \frac{\sqrt{3}\sigma_1 l^3}{4E_s t_2^3}, \tag{19}$$

and the elastic modulus of the hexagonal lattice is $E_1 = \sigma_1/\epsilon_1$, which yields:

$$E_1 = \frac{81}{2}\left[\frac{1}{\bar{t}+2}\right]^3\bar{\rho}^3E_s. \tag{20}$$

When the hexagonal lattice is compressed along the x_1 direction, three collapse modes are possible: (i) elastic buckling of bar 1, (ii) yielding in bar 1, and (iii) plastic collapse in bar 2. The axial force in bar 1 is:

$$T_1 = \sqrt{3}\sigma_1 bl, \tag{21}$$

and elastic buckling will occur when T_1 is equal to the Euler buckling load, which gives:

$$\sigma_{1,el}^{[t_1]} = \frac{27n^2\pi^2}{32}\left[\frac{\bar{t}}{\bar{t}+2}\right]^3\bar{\rho}^3E_s. \tag{22}$$

Again, the end constraint n varies with $\bar{t}$ and its value is derived in Appendix A.2. Next, the stress causing yielding in bar 1 is obtained by setting $T_1 = \sigma_{ys}bt_1$ and this returns:

$$\sigma_{1,pl}^{[t_1]} = \frac{3}{2}\left[\frac{\bar{t}}{\bar{t}+2}\right]\bar{\rho}\sigma_{ys}. \tag{23}$$

Plastic collapse in bar 2 will occur when the bending moment reaches the fully plastic moment $M_p = \sigma_{ys}bt^2/4$. Adapting the expression of Gibson and Ashby [44] gives us:

$$\sigma_{1,pl}^{[t_2]} = \frac{9}{2}\left[\frac{1}{\bar{t}+2}\right]^2\bar{\rho}^2\sigma_{ys}. \tag{24}$$

Finally, the collapse mode associated with the lowest stress will dictate the compressive strength of the lattice:

$$\sigma_1 = \min\left(\sigma_{1,el}^{[t_1]}, \sigma_{1,pl}^{[t_1]}, \sigma_{1,pl}^{[t_2]}\right). \tag{25}$$

2.2.2. Loading in x_2 direction

When the hexagonal lattice is loaded by a uniform compressive stress σ_2 in the x_2 direction, it deforms by bending bar 2. The nominal compressive strain is obtained by adapting the result of Gibson and Ashby [44], which gives:

$$\epsilon_2 = \frac{\sqrt{3}\sigma_2 l^3}{4E_s t_2^3}. \tag{26}$$

The elastic modulus in the x_2 direction becomes:

$$E_2 = \frac{81}{2}\left[\frac{1}{\bar{t}+2}\right]^3\bar{\rho}^3E_s. \tag{27}$$

Comparing this result to Eq. (20) reveals that the hexagonal lattice has the same elastic modulus in both x_1 and x_2 directions.

For compression in the x_2 direction, there is a single failure mode: plastic collapse in bar 2. Therefore, by adapting the expression of Gibson and Ashby [44], we find that the compressive strength σ_2 of the hexagonal lattice is:

$$\sigma_2 = \sigma_{2,pl}^{[t_2]} = \frac{9}{2}\left[\frac{1}{\bar{t}+2}\right]^2\bar{\rho}^2\sigma_{ys}. \tag{28}$$

Finally, note that all analytical expressions presented in this section are in agreement with previous work done by Gibson and Ashby [44] and Wang and McDowell [45]: the properties of uniform triangular and hexagonal lattices can be recovered by setting $\bar{t} = 1$, whereas those of expanded honeycombs (with double thickness vertical walls) can be retrieved with $\bar{t} = 2$.

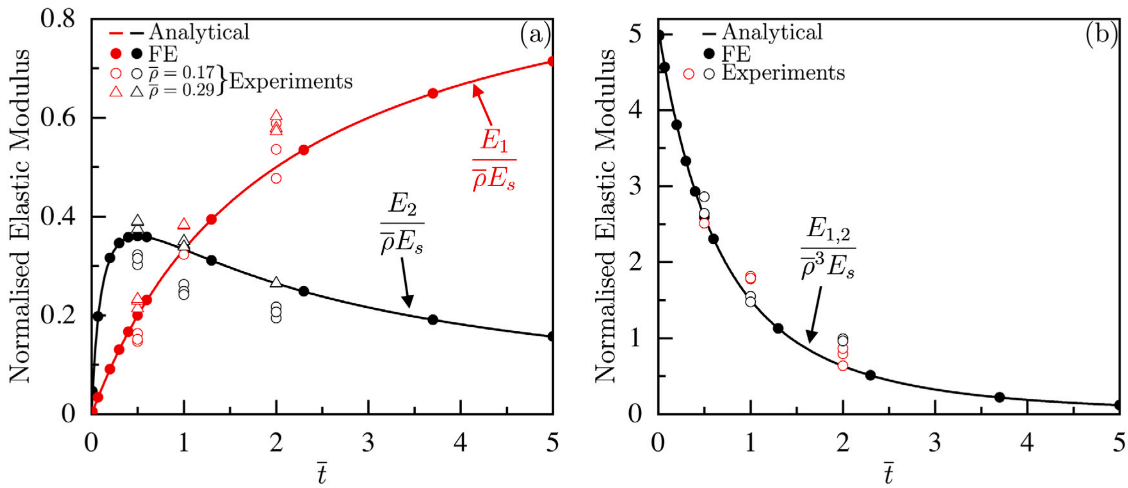

Fig. 2. Normalised elastic modulus as a function of $\bar{t} = t_1/t_2$ for (a) triangular and (b) hexagonal lattices. The modulus E_1 is in red, and E_2 is in black.

3. Analytical results

Analytical results are presented in this section to quantify the effect of $\bar{t}$ on the elastic modulus, collapse mode and compressive strength of both triangular and hexagonal lattices.

3.1. Elastic modulus

The effect of $\bar{t}$ on the elastic modulus of the triangular lattice is shown in Fig. 2a. The elastic modulus E_1 is plotted in red, whereas E_2 is in black. The triangular lattice is stretching-dominated and therefore, both moduli are normalised by $\bar{\rho} E_s$. Consequently, the results are independent of the relative density $\bar{\rho}$ and of the choice of parent material (E_s), see Eq. (5), (13).

The results in Fig. 2a show that E_1 increases monotonically with increasing $\bar{t}$. On the other hand, the elastic modulus E_2 reaches a maximum value of $0.36\bar{\rho} E_s$ at $\bar{t} = 0.5$, which corresponds to $t_2 = 2t_1$. This peak was anticipated since the axial force $T_2 = -2T_1$, see Eq. (10). The main advantage offered by $\bar{t}$ is the possibility to vary the elastic modulus of the lattice while keeping its relative density $\bar{\rho}$ fixed. For the triangular lattice, E_1 can be varied over a wide range of values, increasing more than five-fold when $\bar{t}$ is varied from 0.25 to 3. Of course, increasing E_1 by increasing $\bar{t}$ also leads to a reduction in E_2. Note, however, that E_1 increases more rapidly than E_2 decreases for $\bar{t} > 0.5$. For example, compare the elastic moduli of a triangular lattice with $\bar{t} = 3$ to those of a conventional lattice with $\bar{t} = 1$. The lattice with $\bar{t} = 3$ has a modulus E_1 80% higher than that with $\bar{t} = 1$, whereas the reduction in E_2 is only 35%. Therefore, the trade-off between E_1 and E_2 can be advantageous.

The elastic modulus of the hexagonal lattice is plotted as a function of $\bar{t}$ in Fig. 2b. The hexagonal lattice is bending-dominated and therefore its elastic modulus is normalised by $\bar{\rho}^3 E_s$ to ensure that the results are insensitive to both $\bar{\rho}$ and E_s, see Eq. (20), (27). In contrast with the triangular lattice, the hexagonal topology has the same elastic modulus in both directions, see Eq. (20) and (27). In addition, the elastic modulus increases monotonically as $\bar{t}$ decreases. These two observations can be explained by the fact that the hexagonal lattice deforms primarily by bending bar 2 when loaded along either x_1 or x_2. Again, varying $\bar{t}$ allows to change the elastic modulus over a wide range of values: E_1 and E_2 change by an order of magnitude when $\bar{t}$ varies from 0.25 to 3. Note that the effect of $\bar{t}$ on the elastic modulus is more important for the hexagonal lattice than for the triangular topology. This is because the expression of E_1 for the hexagonal lattice contains terms in $\bar{t}^3$, whereas for triangular lattice E_1 contains only terms in $\bar{t}$.

3.2. Collapse modes

Failure maps are presented in Fig. 3 to illustrate how the collapse mode changes as a function of $\bar{\rho}$ and $\bar{t}$. These maps are sensitive to the choice of parent material, and the results in Fig. 3 are for $E_s = 200$ GPa and $\sigma_{ys} = 250$ MPa, which is representative of structural steel.

Two collapse modes are possible when the triangular lattice is compressed in x_1: elastic buckling or yielding of bar 1, see Fig. 3a. As expected, elastic buckling is predominant at low values of relative density (less than $\bar{\rho} \approx 0.07$) and when $\bar{t}$ is inferior to approximately 0.25. On the other hand, three collapse modes can occur when the triangular lattice is compressed in x_2: elastic buckling in bar 2, and yielding of bar 1 or 2, see Fig. 3b. Again, elastic buckling takes place at low values of relative density. Yielding takes place in bar 1 when $\bar{t} < 0.5$, and in bar 2 otherwise.

Failure maps for the hexagonal lattice are given in Fig. 3c and d for compression in x_1 and x_2, respectively. In both directions, most geometries fail by plastic collapse of bar 2. For compression in x_1, the hexagonal lattice can also fail by elastic buckling or yielding of bar 1, but these modes are active only for very low values of $\bar{\rho}$ or $\bar{t}$.

Finally, the influence of the parent material on the collapse mode can be evaluated by comparing Fig. 3 to 4, where the failure maps are plotted for $E_s = 2.4$ GPa and $\sigma_{ys} = 41$ MPa. These material properties are those of a polymer, which will be used in the experiments reported below (Section 5). For both lattices, changing the parent material from steel to a polymer significantly expands the predominance of elastic buckling. This is particularly striking for the triangular lattice, where nearly all geometries fail by elastic buckling when the parent material is a polymer.

3.3. Compressive strength

The influence of $\bar{t}$ on the compressive strength is shown in Fig. 5 for the triangular lattice and in Fig. 6 for the hexagonal topology. In both figures, the results are given for steel lattices ($E_s = 200$ GPa and $\sigma_{ys} = 250$ MPa) with $\bar{\rho} = 0.001$ (in part a) and $\bar{\rho} = 0.2$ (in part b). These two values of relative density were selected to cover all failure modes for steel lattices, see Fig. 3.

Triangular lattices with $\bar{\rho} = 0.001$ fail by elastic buckling in both x_1 and x_2 directions, see Fig. 3. Accordingly, the compressive strength is normalised by $\bar{\rho}^3 E_s$ in Fig. 5a; therefore, the results are valid for any triangular lattice that fails by elastic buckling, see Eq. (7), (14). The compressive strength σ_1 increases with increasing $\bar{t}$, whereas σ_2 decreases with increasing $\bar{t}$. The failure mode of triangular lattices switches to yielding when its relative density is increased to $\bar{\rho} = 0.2$,

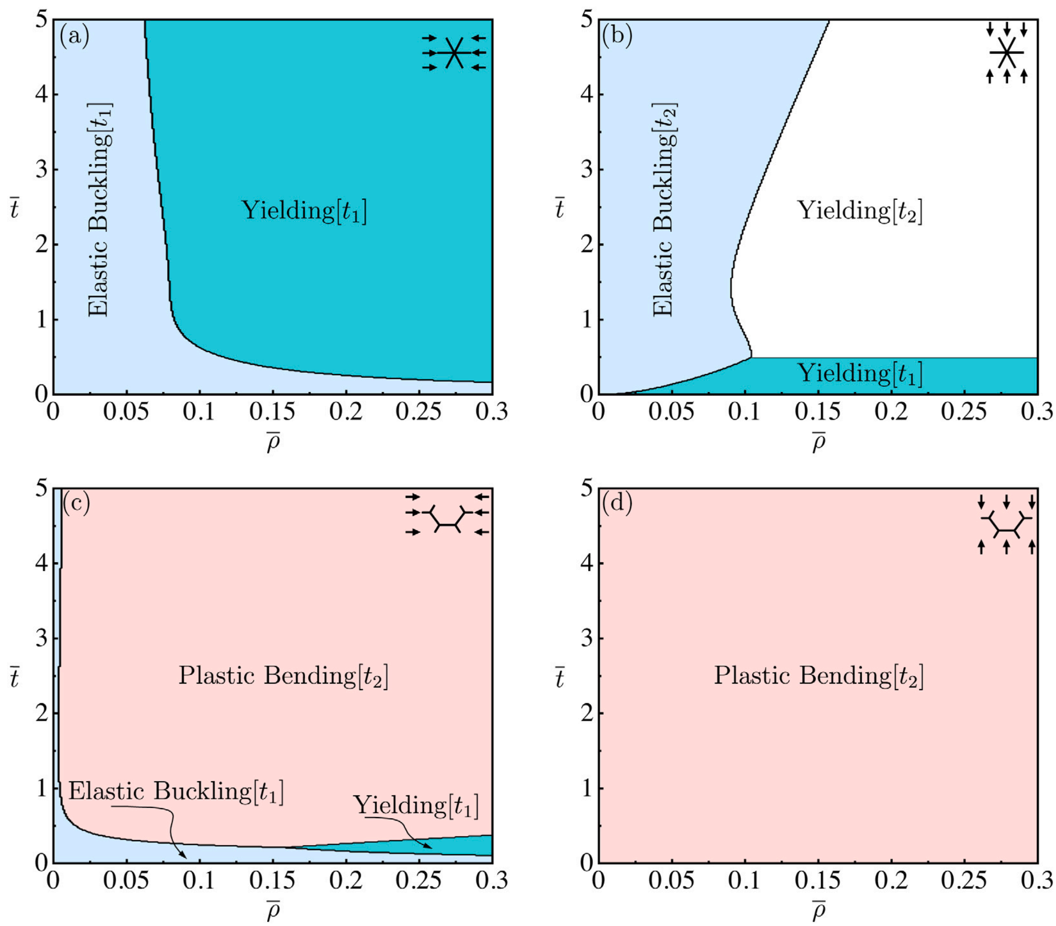

Fig. 3. Failure maps for prismatic lattices made from steel ($E_s = 200$ GPa and $\sigma_{ys} = 250$ MPa). Results are given for the triangular lattice compressed in (a) x_1 and (b) x_2; and the hexagonal lattice compressed in (c) x_1 and (d) x_2.

see Fig. 3. Consequently, its compressive strength has been normalised by $\bar{\rho}\sigma_{ys}$ in Fig. 5b to ensure that the results are representative of any triangular lattice that fails by yielding, see Eq. (8), (15), (16). The compressive strength σ_1 increases with increasing $\bar{t}$, but, in contrast, σ_2 exhibit a peak strength $\sigma_{2,pk} = 0.6\bar{\rho}\sigma_{ys}$ when $\bar{t} = 0.5$. This peak is associated with a change in failure mode: yielding occurs in bar 1 for $\bar{t} < 0.5$ and in bar 2 otherwise, see Fig. 3.

The compressive strength of an hexagonal lattice with $\bar{\rho} = 0.001$ is shown in Fig. 6a, where results are plotted on a double y-axis. On the left axis, σ_1 is normalised by $\bar{\rho}^3 E_s$ because the lattice fails by elastic buckling, see Fig. 3c. On the right axis, σ_2 is normalised by $\bar{\rho}^2\sigma_{ys}$ since the hexagonal lattice collapses by plastic bending, see Fig. 3d. These normalisations are based on Eq. (22) and (28) to ensure that the results are insensitive to $\bar{\rho}$ and the material properties (as long as the failure modes remain unchanged). Clearly, σ_2 increases monotonically with decreasing $\bar{t}$. In contrast, the strength along x_1 displays a peak $\sigma_{1,pk} = 0.147\bar{\rho}^3 E_s$ at $\bar{t} = 1.11$. This peak is the result of two competing effects. On one hand, increasing $\bar{t}$ increases the elastic buckling resistance according to Eq. (22). On the other hand, the end constraint n decreases with increasing $\bar{t}$: n decreases from 1 to 0.1 when $\bar{t}$ varies from 0 to 5, see Appendix A.2.

Finally, the compressive strength of the hexagonal lattice with $\bar{\rho} = 0.2$ is plotted in Fig. 6b, There are three different collapse modes when $\bar{\rho} = 0.2$ (see Fig. 3c) and therefore it is impossible to have a unique normalisation in this case. Consequently, both σ_1 and σ_2 are normalised by σ_{ys} in Fig. 6b. The hexagonal lattice has the same strength in both directions when $\bar{t} \geq 0.27$ because plastic collapse of bar 2 is the operative failure mode, see Fig. 3c,d. For this failure mode, the compressive strength ($\sigma_1 = \sigma_2$) increases with decreasing $\bar{t}$. Then, when $\bar{t} < 0.27$, σ_1 decreases with decreasing $\bar{t}$, and this is due to a change in failure mode, see Fig. 3c.

4. Finite element simulations

4.1. Description of the finite element model

Finite Element (FE) simulations were performed to verify the analytical results presented in Section 3. All simulations were done with the commercial software Abaqus (version 2017) and using the standard solver (Static, Implicit step in Abaqus). Periodic unit cells, shown in Fig. 1, were used for each topology. In all cases, the bar length was kept fixed to $l = 10$ mm, but the bar thicknesses t_1 and t_2 were modified to vary $\bar{\rho}$ and $\bar{t}$. The cell walls were discretised using Timoshenko beam elements (B21 in Abaqus notation): we used 30 elements per bar for the triangular lattice and 70 elements per bar for the hexagonal topology. A mesh convergence study revealed that further mesh refinements had a negligible effect on the results (a difference less than 0.3%). A geometric imperfection was included in all simulations; it had the shape of the first eigenmode and its amplitude was set to 5% of the bar thickness expected to buckle. The parent material was modelled as an elastic perfectly plastic solid. The elastic regime was linear and isotropic, characterised by a Young's modulus $E_s = 200$ GPa and a Poisson's ratio $\nu_s = 0.26$, up to a yield strength $\sigma_{ys} = 250$ MPa.

Periodic boundary conditions were imposed with the following constraint equations [69,70]:

$$\Delta u_i = \epsilon_{ij}\Delta x_j \quad \text{and} \quad \Delta\phi = 0, \tag{29}$$

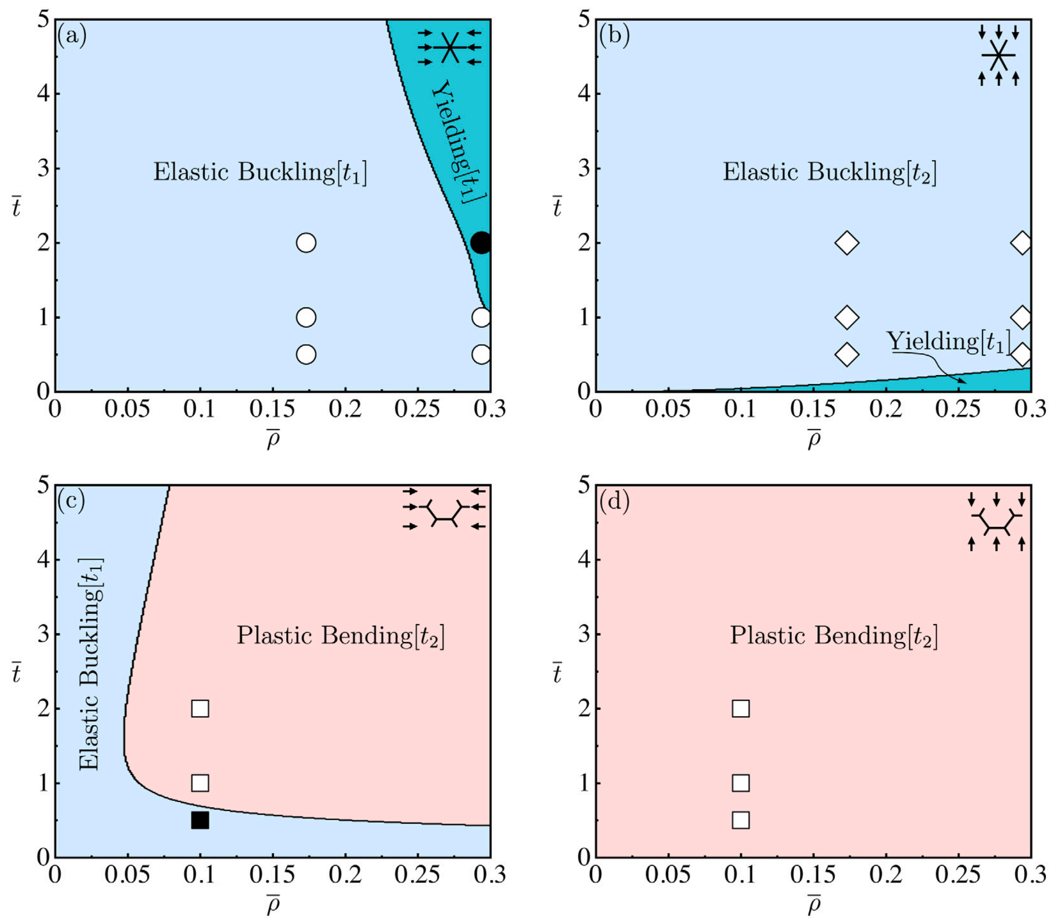

Fig. 4. Failure maps for prismatic lattices made from a polymer ($E_s = 2.4$ GPa and $\sigma_{ys} = 41$ MPa). Results are given for the triangular lattice compressed in (a) x_1 and (b) x_2; and the hexagonal lattice compressed in (c) x_1 and (d) x_2. The geometries tested are marked with different symbols depending on the failure mode. In all cases, the observed failure modes were in agreement with our analytical predictions.

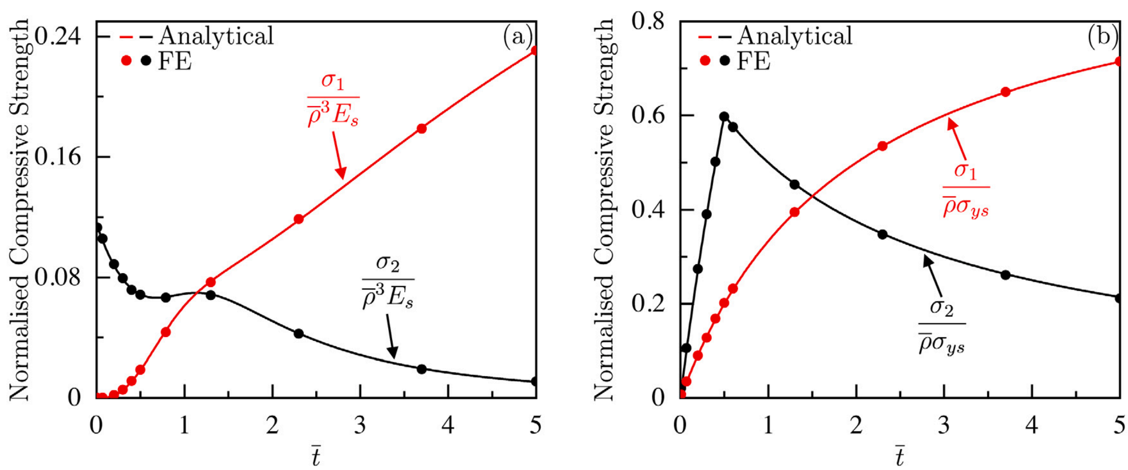

Fig. 5. Normalised compressive strength as a function of $\bar{t} = t_1/t_2$ for a triangular lattice with (a) $\bar{\rho} = 0.001$ and (b) $\bar{\rho} = 0.2$. The strength σ_1 is in red, and σ_2 is in black. The parent material is steel: $E_s = 200$ GPa and $\sigma_{ys} = 250$ MPa.

where Δu_i and $\Delta\phi$ are the difference in displacement and rotation, respectively, between corresponding points of the unit cell; ϵ_{ij} is the macroscopic nominal strain tensor; and Δx_j is the displacement vector connecting two corresponding points of the unit cell. The compressive response of the lattice along x_1 was obtained by prescribing the value of ϵ_{11}, and the work conjugate σ_{11} was calculated by Abaqus assuming that $\sigma_{22} = 0$. Likewise, the compressive response along x_2 was obtained by imposing ϵ_{22}, and computing σ_{22} provided that $\sigma_{11} = 0$.

4.2. Comparison between simulations and analytical results

Finite Element predictions for E_1 and E_2 are compared to analytical results in Fig. 2 for both triangular and hexagonal lattices. The FE data was obtained for $\bar{\rho} = 0.001$, but the normalisation used in Fig. 2 is such that the results are insensitive to the choice of relative density even up to $\bar{\rho} = 0.2$. Clearly, there is an excellent agreement between FE simulations and analytical equations for both E_1 and E_2, and over the

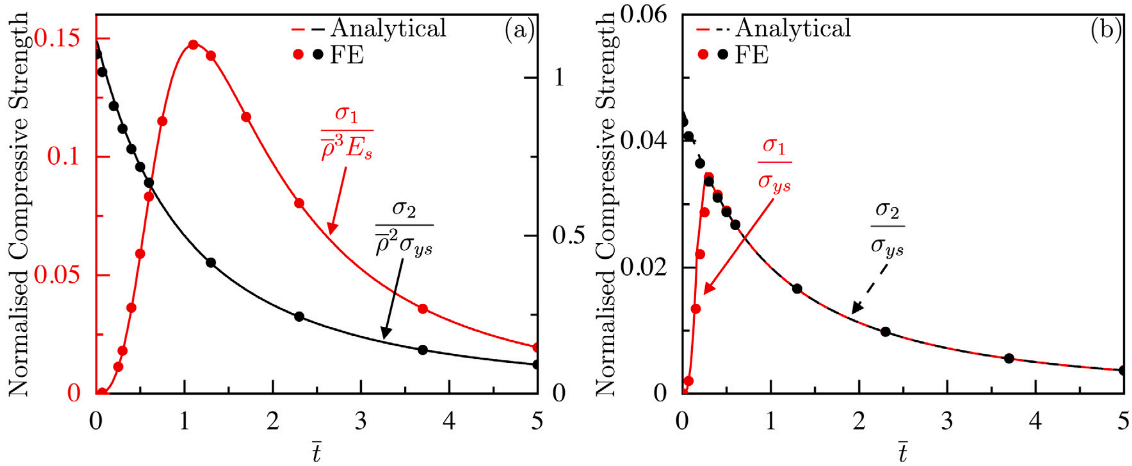

Fig. 6. Normalised compressive strength as a function of $\bar{t} = t_1/t_2$ for a hexagonal lattice with (a) $\bar{\rho} = 0.001$ and (b) $\bar{\rho} = 0.2$. The strength σ_1 is in red, and σ_2 is in black. The parent material is steel: $E_s = 200$ GPa and $\sigma_{ys} = 250$ MPa.

entire range of $\bar{t}$ considered here. This is true for both triangular and hexagonal topologies.

Next, FE predictions of the compressive strength are compared to analytical results in Figs. 5 and 6 for triangular and hexagonal lattices, respectively. In both figures, there is an excellent agreement between FE and analytical results. In all cases, the failure mode predicted analytically corresponded to the one observed in FE simulations. Based on the results shown in Figs. 2, 5 and 6, we conclude that the analytical expressions derived in Section 2 are validated by FE simulations.

5. Experiments

Experiments were also conducted to assess the accuracy of the analytical predictions derived in Section 2. The procedure used to manufacture the samples is described below. Then, the measured responses and observed failure modes are reported. Finally, the experimental results are compared to our analytical predictions.

5.1. Specimen manufacture

All samples were fabricated by additive manufacturing; more specifically, using a Formlabs Form 2 machine, which uses stereolithography to cure a photo-polymerising resin. Both triangular and hexagonal lattices were manufactured and their dimensions are given in Fig. 7. Lattice materials exhibit size effects, but the number of cells in each sample is sufficiently large to ensure that the elastic modulus is within 12% of the infinite bulk limit [46,71]. For each topology, three specimens were prepared with $\bar{t} = 0.5$, 1, and 2, while keeping the relative density fixed. This was done by varying the bar thicknesses t_1 and t_2 as indicated in Table 1, and keeping the bar length fixed at $l = 10$ mm. In all cases, the specimens had a depth of 15 mm in the prismatic direction. Tests were conducted in both x_1 and x_2 directions, and the geometries are indicated on the failure maps presented earlier in Fig. 4.

The specimens were fabricated as follows. First, the geometry of the sample was created in Abaqus and a stl file was exported to the Form 2 machine. Second, the specimen was printed with a layer thickness of 0.025 mm and using the Formlabs Clear resin. All samples were printed with their prismatic axis perpendicular to the printing bed. Finally, when the print was completed, the lattice was washed in an isopropyl alcohol (IPA) solution and post-cured under UV light at a temperature of 60 °C for 30 min, as recommended in the Formlabs documentation.

Tensile tests were conducted to characterise the behaviour of the Clear resin used to manufacture the lattices. Following the procedure detailed above, dog-bone specimens were fabricated with a gauge length of 33 mm and a width of 6 mm, in accordance with the standard test method for tensile properties of plastics (ASTM D638-14). Ten tests were performed: five with a thickness of 1.5 mm and five with a thickness of 3 mm. The tensile response was, however, insensitive to the thickness of the dog-bones. From these ten tensile tests, conducted at 10^{-3} s^{-1}, the average material properties and their standard deviation were: a Young's modulus $E_s = 2.43 \pm 0.18$ GPa, a 0.2% yield strength $\sigma_{ys} = 40.9 \pm 2.4$ MPa, and an ultimate tensile strength of 62.0 ± 2.4 MPa. These values are close to those reported by Formlabs (which are a Young's modulus of 2.80 GPa and an ultimate tensile strength of 65 MPa). Finally, a measured stress–strain curve is given in Fig. 8; this test had properties very close to the averages given above.

Table 1
Values of relative density $\bar{\rho}$ and thickness ratio $\bar{t}$ covered in the experiments.

Topology	$\bar{\rho}$	$\bar{t}$	t_1 [mm]	t_2 [mm]
Triangular	0.17	0.5	0.30	0.60
		1	0.50	0.50
		2	0.75	0.38
	0.29	0.5	0.51	1.02
		1	0.85	0.85
		2	1.28	0.64
Hexagonal	0.10	0.5	0.52	1.04
		1	0.87	0.87
		2	1.30	0.65

5.2. Compressive responses and collapse modes

The printed specimens had no visible imperfections, such as broken or wavy bars. All samples were tested in compression using a MTS electromechanical testing machine with a capacity of 30 kN. The lattices were crushed at a constant rate of 0.05 mm/s, corresponding to a nominal strain rate of approximately $7 \cdot 10^{-4}$ s^{-1}. Both the compressive force and displacement were recorded by the testing machine.

The compressive responses of triangular lattices with $\bar{\rho} = 0.17$ are shown in Fig. 9a and b for compression along x_1 and x_2, respectively. In each plot, responses for $\bar{t} = 0.5$, 1 and 2 are compared. All samples had a linear elastic regime up to a peak stress, followed by a gradually softening response. To show the failure modes, photographs of all tests are given in Fig. 10. All specimens compressed in the x_1 direction failed by elastic buckling of bar 1. In contrast, elastic buckling occurred in bar 2 for all triangular lattices loaded in x_2. These failure modes are in agreement with our analytical predictions, see the failure maps in Fig. 4a, b.

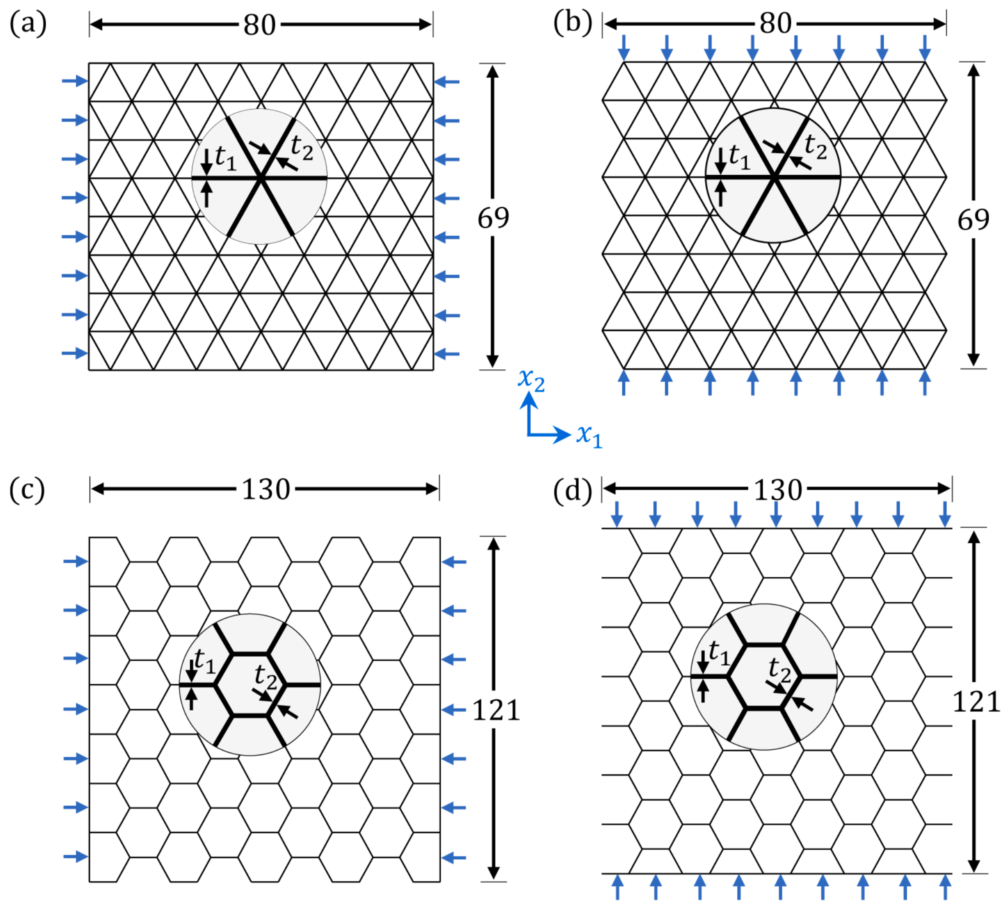

Fig. 7. Dimensions of the samples tested: triangular lattice compressed in (a) x_1 and (b) x_2; and hexagonal lattice compressed in (c) x_1 and (d) x_2. All samples had a bar length l = 10 mm and a depth of 15 mm in the prismatic direction. All dimensions are in mm.

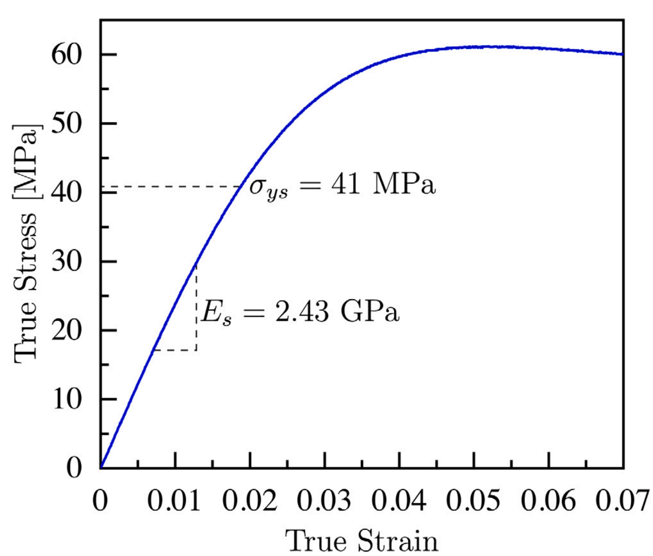

Fig. 8. Tensile response of the polymer used to manufacture all samples.

The measured responses for the hexagonal lattice compressed in x_1 are shown in Fig. 9c. The sample with $\bar{t}$ = 0.5 has a linear elastic response up to the peak stress. This specimen failed by elastic buckling of bar 1, see the photograph given in Fig. 11a. This is the same buckling mode observed previously for uniform honeycombs [44]. In contrast, the response of specimens with $\bar{t}$ = 1 and 2 was characterised by an initial linear elastic regime, followed by a non-linear regime, before reaching the peak stress. These geometries failed by plastic collapse of bar 2, see Fig. 11b, c, where localisation begins at the centre of the specimen. This deformation mode is practically identical to the one observed previously for expanded metallic honeycombs [49,50]. Similarly, all samples failed by plastic collapse of bar 2 when the hexagonal lattice was compressed in x_2, see the responses in Fig. 9d and photographs in Fig. 11d,e,f. The failure modes observed for the hexagonal lattice are in agreement with the maps presented earlier in Fig. 4c, d.

5.3. Comparison between experiments and analytical/FE predictions

The measured elastic moduli are compared to our analytical predictions in Fig. 2. There are multiple data points since the majority of our tests were repeated three times to assess their variability. The experimental scatter is low; in fact, the relative deviation is inferior to 10% for 92% of our tests. For both lattices, there is a good agreement between the measured and analytical values of E_1 and E_2. The largest discrepancy is observed for the elastic modulus E_1 of triangular lattices with $\bar{\rho}$ = 0.29 and $\bar{t}$ = 2, where the measurements are on average 17% higher than the analytical prediction. This is mainly due to a size effect: when the number of cells n across the width of triangular lattice is small, its modulus E_1 is $(n + 1)/n$ times higher than its asymptotic value [46]. In our experiments, n = 8 and therefore, the modulus E_1 is 12.5% higher due to this size effect. Considering this, the difference between experiments and analytical prediction is less than 5%.

Next, the measured compressive strength is compared to our analytical results in Fig. 12. Here, the compressive strength is normalised by the yield strength of the parent material σ_{ys} = 41 MPa. Again, the

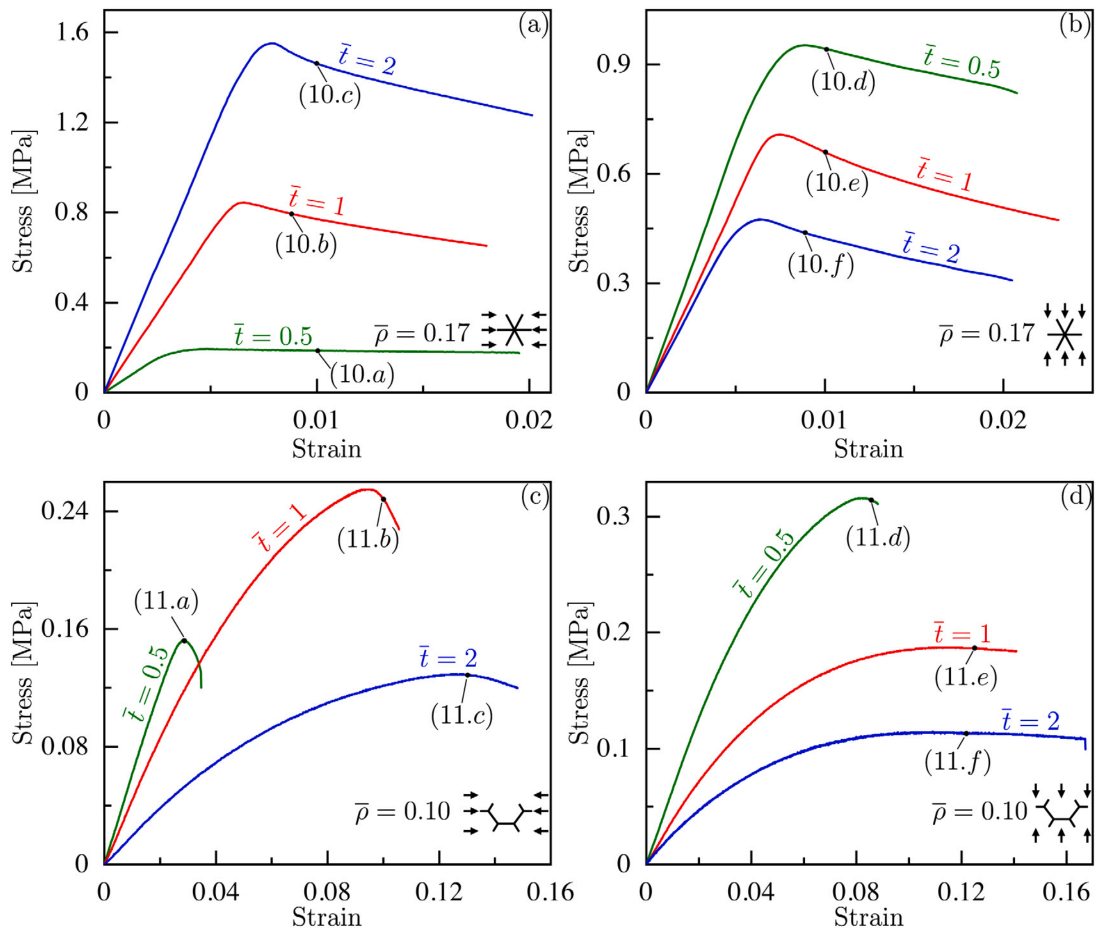

Fig. 9. Measured responses for the triangular lattice compressed in (a) x_1 and (b) x_2; and the hexagonal lattice compressed in (c) x_1 and (d) x_2.

scatter is small on the measured compressive strength; 86% of our tests have a relative deviation of less than 10%. The largest discrepancy between experimental and analytical results is observed for the triangular lattice compressed in x_1 with $\bar{\rho} = 0.29$ and $\bar{t} = 2$, see Fig. 12b. This sample is expected to fail by yielding (see the map in Fig. 4a) and a factor that may explain the discrepancy is the fact that the polymer used in the experiments has a strain hardening response (see Fig. 8) which is neglected in the analytical model. Furthermore, the discrepancies are not attributed to the fact that our analytical model neglects the stress concentrations at the nodes. To reach this conclusion, we compared the results of 2D plane stress simulations (not reported here) with those obtained with beam elements and found a negligible difference between the two approaches. Nonetheless, there is, for both topologies, a reasonable agreement between the measured compressive strength and the analytical predictions shown in Fig. 12.

Finally, the observed deformation modes are compared to FE simulations in Figs. 10 and 11 for the triangular and hexagonal lattices, respectively. Recall that FE simulations were done using beam elements, but their profile was rendered in Figs. 10 and 11 for visualisation purposes only. For both topologies, there is a good agreement between the observed and simulated deformation modes. This is true for all values of $\bar{t}$ and for both loading directions.

6. Discussion

In this paper, we introduced a new parameter $\bar{t}$ to customise the in-plane properties of triangular and hexagonal lattices. The thickness ratio $\bar{t}$ does not affect the behaviour of a lattice (whether is it stretching- or bending-dominated) but it does increase the number of possible failure modes (there is an additional failure mode for both triangular and hexagonal lattices). The main advantage of $\bar{t}$ is that it enables to vary the mechanical properties of a lattice without changing its density. This is illustrated in Fig. 13, where the normalised elastic modulus E_1/E_s and the normalised strength σ_1/σ_{ys} of the triangular lattice are plotted as a function of relative density and for selected values of $\bar{t}$. Both E_1 and σ_1 increase monotonically with increasing $\bar{t}$ and therefore, the maximum increase in performances will depend on the highest value of $\bar{t}$ that can be manufactured. Using a fairly conservative estimate that $t_1 = 5t_2$ already leads to significant increases in properties: a triangular lattice with $\bar{t} = 5$ is more than two times stiffer and up to 3.8 times stronger than a conventional design with $\bar{t} = 1$, see Fig. 13.

The properties of the hexagonal lattice can also be increased by varying $\bar{t}$. For this topology, however, it is E_2 and σ_2 that increase monotonically with decreasing $\bar{t}$, see Fig. 14. Again, varying the bar thickness by a factor of 5 ($t_2 = 5t_1 \Rightarrow \bar{t} = 0.2$) can lead to significant changes in properties: a hexagonal lattice with $\bar{t} = 0.2$ is more than 2.5 times stiffer and 1.8 times stronger than its counterpart with $\bar{t} = 1$.

The results in Figs. 13 and 14 show how the properties along a specific direction can be increased by varying $\bar{t}$, and this is ideal for applications where the load is concentrated in a single direction. Increasing the properties along one direction, however, tends to reduce the properties in the perpendicular direction. This can be used in an advantageous way: $\bar{t}$ can be used to control the degree of anisotropy of a lattice. Elastic anisotropy is usually quantified using the Zener index [72], but it requires components of the elasticity tensor that were outside the scope of this work. To overcome this, we propose to quantify anisotropy here using the ratio E_1/E_2, which has an intuitive physical meaning. For the triangular lattice, the anisotropy ratio E_1/E_2

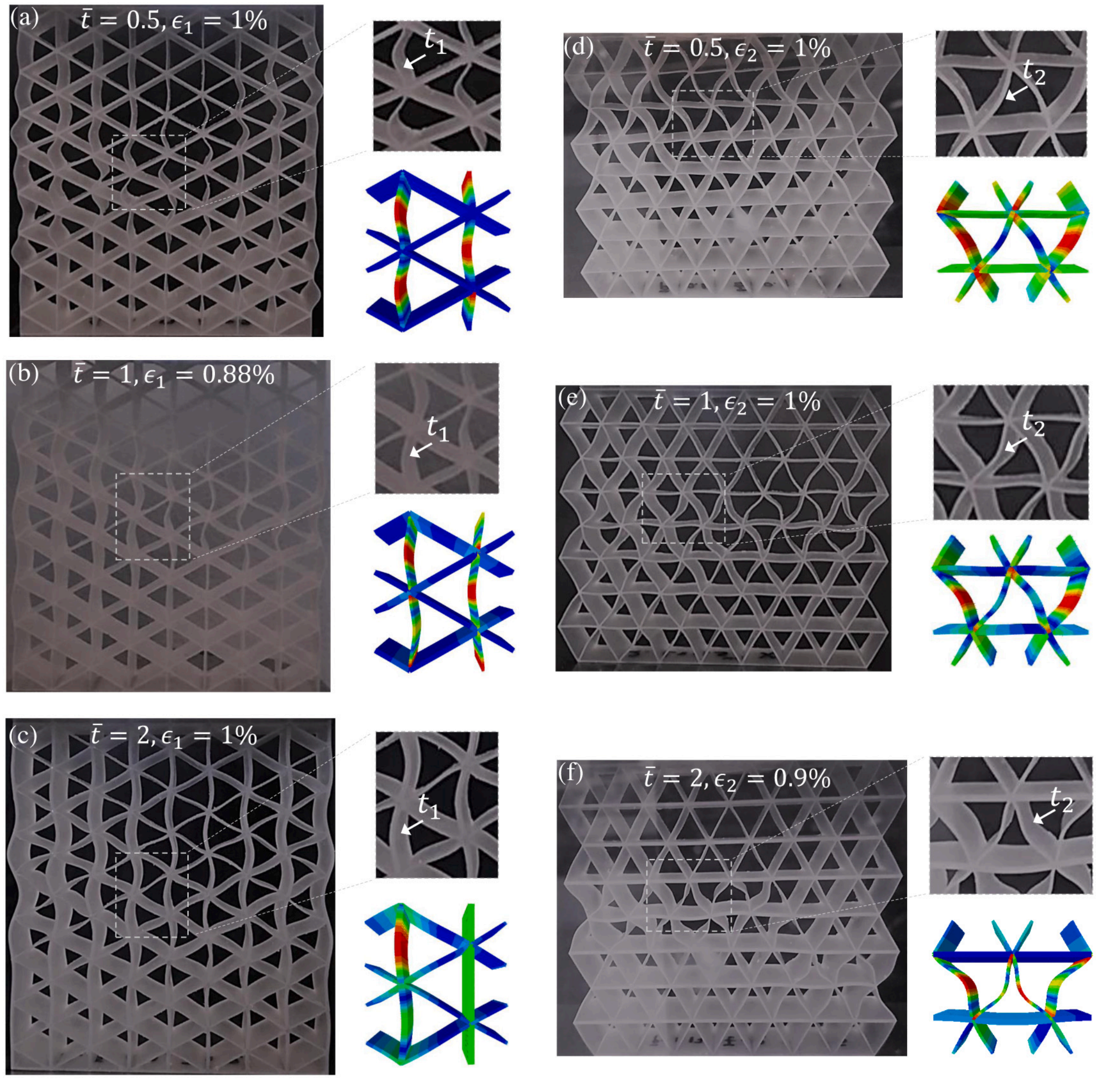

Fig. 10. Photographs showing the failure modes of a triangular lattice with $\bar{\rho} = 0.17$ and selected values of $\bar{t}$. All samples compressed in x_1 (left column) fail by elastic buckling of bar 1, whereas those compressed in x_2 (right column) fail by elastic buckling of bar 2. The instant when each photograph was taken is indicated in Fig. 9a, b. For scale, all bars have a length of 10 mm. The deformation modes obtained from FE simulations using beam elements are also included for comparison.

of the can be obtained by dividing Eq. (5) by (13), which yields:

$$\frac{E_1}{E_2} = \frac{8\bar{t} + 1}{9}. \tag{30}$$

Therefore, the anisotropy ratio E_1/E_2 varies linearly with $\bar{t}$. This relationship is plotted in Fig. 15 and it is reasonably well corroborated by our experiments. Recall that conventional triangular lattices with $\bar{t} = 1$ are transversely isotropic, $E_1 = E_2$ [44,45,70]. Introducing $\bar{t}$, however, expands the design space and allows us to create lattices with a wide range of E_1/E_2, see Fig. 15. Unfortunately, this advantage is limited to the triangular lattice since $E_1 = E_2$ for the hexagonal lattice, see Eq. (20) and (27).

Finally, it is important to note that even though our analysis focused on triangular and hexagonal lattices, the concept proposed in this paper is applicable to other topologies. For example, we show in Supplementary material how the same approach can be applied to a kagome lattice. The concept could also be extended to three-dimensional lattices such as the octet truss. For 3D topologies, all bars in a given plane would have a diameter d_1 whereas others would have a diameter d_2, and therefore, the properties could be adjusted by controlling the ratio d_1/d_2.

7. Conclusions

We examined the performances of prismatic lattices with cell walls having two different thicknesses. The ratio of these two thicknesses introduced a new design parameter $\bar{t}$. The influence of $\bar{t}$ on the mechanical properties of triangular and hexagonal lattices was first investigated analytically. Then, these analytical expressions were (i) validated using finite element simulations, and (ii) corroborated by experiments conducted on polymer samples produced by additive manufacturing.

The results showed that this new parameter $\bar{t}$ can be used to vary the properties of a lattice while keeping its relative density fixed. The thickness ratio also controlled the degree of anisotropy: varying $\bar{t}$ typically increased the properties in one direction but reduced them in the perpendicular direction. Our analysis indicated that this trade-off can be advantageous since the increase in one direction is often more important than the reduction in the other direction. For example, the elastic modulus of the triangular lattice increased by 80% in one direction and decreased by only 35% in the perpendicular direction, when $\bar{t}$ was increased from 1 to 3. In conclusion, the thickness ratio $\bar{t}$ introduced in this paper offers a new way to tailor the properties of prismatic lattices. Our analysis focused on triangular and hexagonal

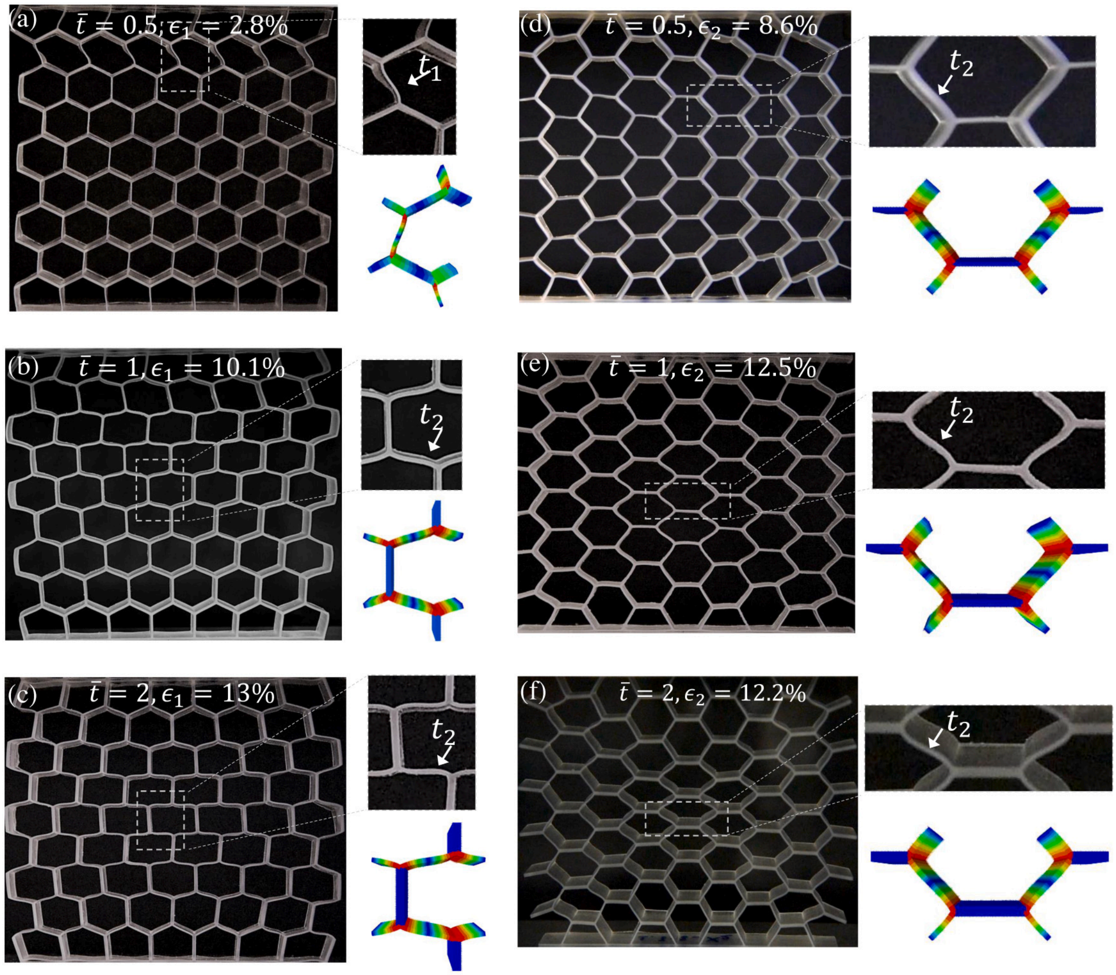

Fig. 11. Photographs showing the failure modes of a hexagonal lattice with $\bar{\rho} = 0.10$ and selected values of $\bar{t}$. Samples compressed in x_1 (left column) and in x_2 (right column) are included. All specimens failed by plastic collapse of bar 2, except $\bar{t} = 0.5$ compressed in x_1 which failed by elastic buckling of bar 1. The instant when each photograph was taken is indicated in Fig. 9c,d. For scale, all bars have a length of 10 mm. The deformation modes obtained from FE simulations using beam elements are also included for comparison.

lattices, but the approach presented here can be extended to other topologies.

CRediT authorship contribution statement

Anastasia Markou: Conceptualization, Methodology, Investigation, Writing – original draft, Visualization. **Luc St-Pierre:** Conceptualization, Supervision, Writing – review & editing, Funding acquisition.

Declaration of competing interest

The authors declare that they have no known competing financial interests or personal relationships that could have appeared to influence the work reported in this paper.

Acknowledgements

AM wishes to thank the School of Engineering of Aalto University for their financial support. LS gratefully acknowledges the financial support from the Academy of Finland (decision 322007). The authors are also thankful to the Aalto University Digital Design Laboratory (ADDlab) and to K. Widell for their technical assistance in manufacturing and testing.

Appendix A. End constraint factor

The elastic buckling strength of hexagonal lattices has been studied extensively for in-plane uniaxial [44,68,73–75] and biaxial [47,48,76–80] compression. The approach employed here is based on a small strain analysis of a perfect periodic unit cell, as in [44,68], and provides an upper bound for the buckling load [76]. Our analysis is similar to that of Fan et al. [68] who derived analytically the end constraint factor n for different prismatic lattices. Their work, however, was limited to lattices with $\bar{t} = 1$, and here we extend their study to capture the influence of $\bar{t}$ on the end constraint factor n.

The method used to calculate n relies on the stiffness matrix of a single bar. Consider a bar of length l loaded by an axial compressive force P, as shown in Fig. A.1a. Next, assume that small rotations θ_a and θ_b are imposed at ends a and b, respectively, and a small transverse displacement Δ is prescribed, see Fig. A.1b. The corresponding bending moments M_a and M_b, and shear force V are given by [67]:

$$\begin{Bmatrix} M_a \\ M_b \\ V \end{Bmatrix} = \frac{E_s I}{l} \begin{bmatrix} s & sc & \bar{s}/l \\ sc & s & \bar{s}/l \\ \bar{s}/l & \bar{s}/l & s^*/l^2 \end{bmatrix} \begin{Bmatrix} \theta_a \\ \theta_b \\ \Delta \end{Bmatrix}, \tag{A.1}$$

where E_s is the elastic modulus and I is the second moment of area of the bar. In addition, $\bar{s}$ and s^* are:

$$\bar{s} = s(1+c) \quad \text{and} \quad s^* = 2\bar{s} - \frac{Pl^2}{E_s I}, \tag{A.2}$$

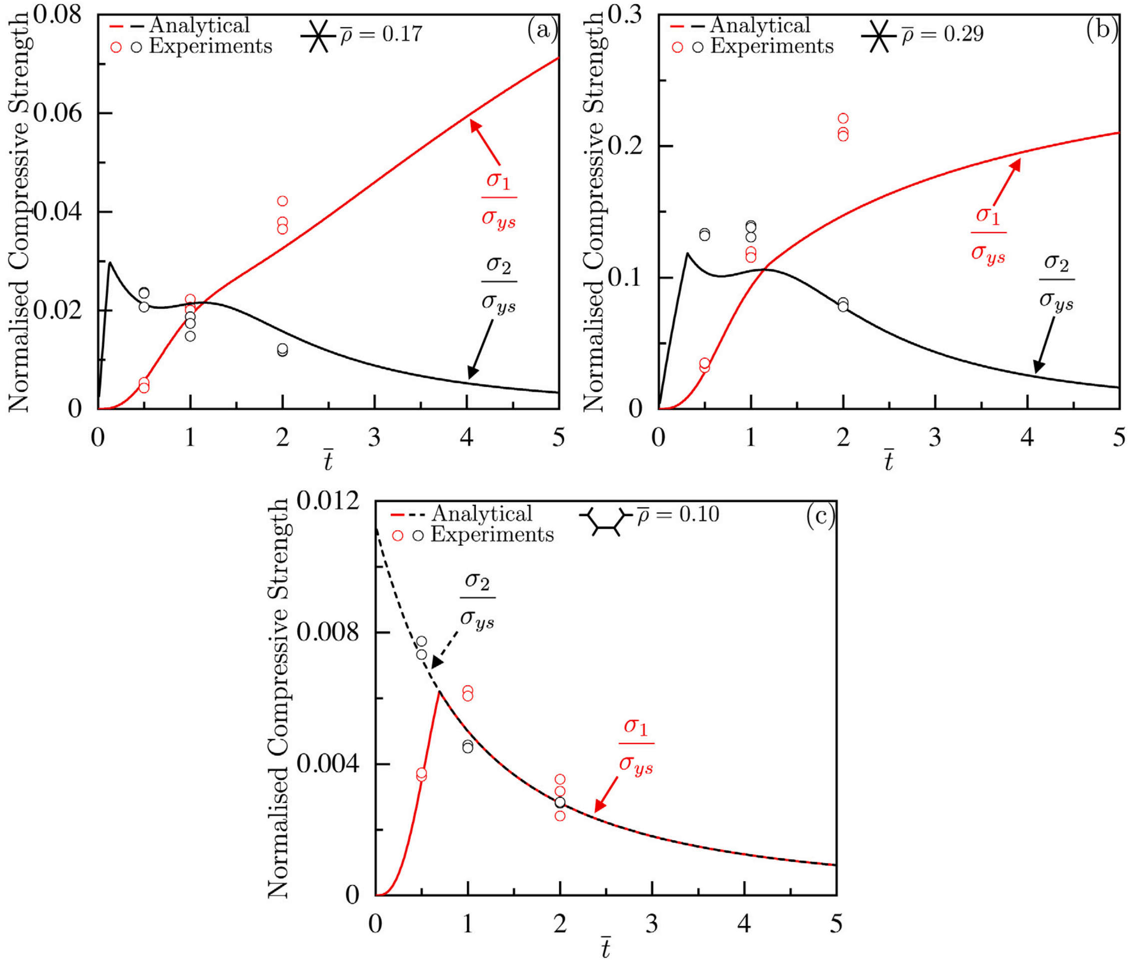

Fig. 12. Comparison between the measured compressive strength and our analytical predictions. Results are given for a triangular lattice with (a) $\bar{\rho} = 0.17$ and (b) $\bar{\rho} = 0.29$; and (c) a hexagonal lattice with $\bar{\rho} = 0.10$.

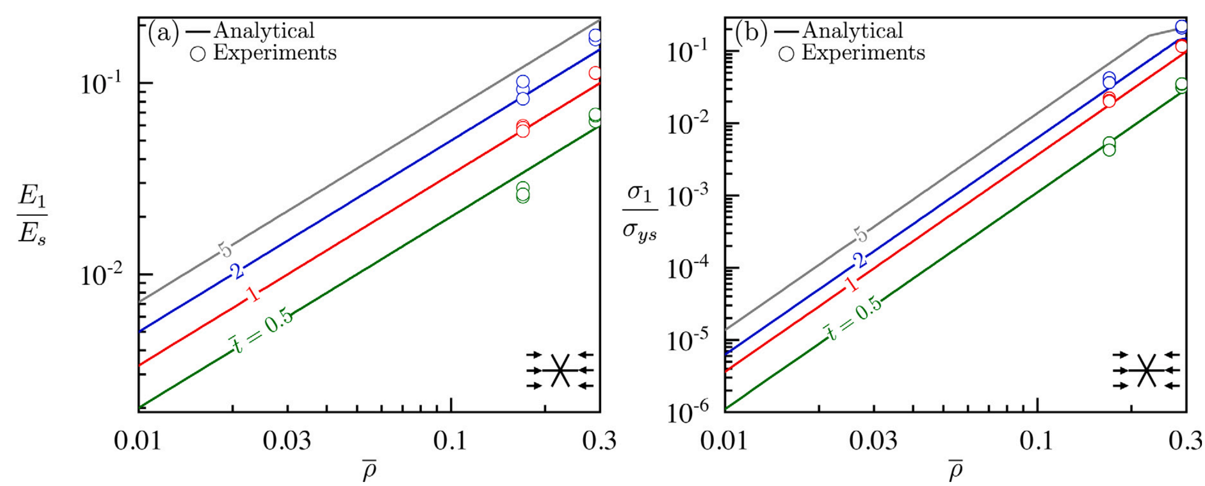

Fig. 13. Properties of the triangular lattice compressed x_1: (a) normalised elastic modulus and (b) normalised strength, both as a function of the relative density $\bar{\rho}$ ($E_s = 2.4\,\mathrm{GPa}$ and $\sigma_{ys} = 41\,\mathrm{MPa}$).

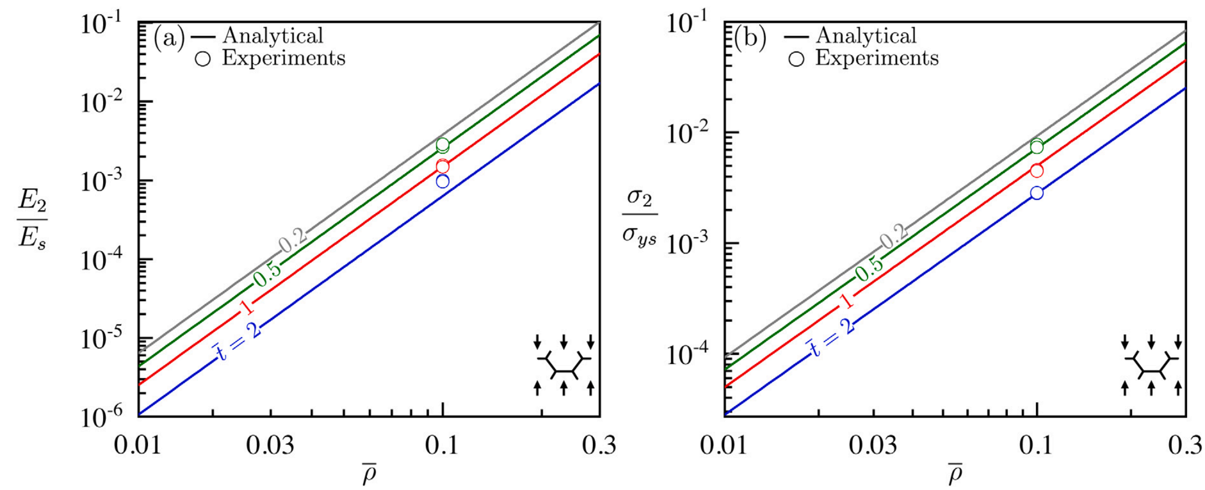

Fig. 14. Properties of the hexagonal lattice compressed x_2: (a) normalised elastic modulus and (b) normalised strength, both as a function of the relative density $\bar{\rho}$ ($E_s = 2.4$ GPa and $\sigma_{ys} = 41$ MPa).

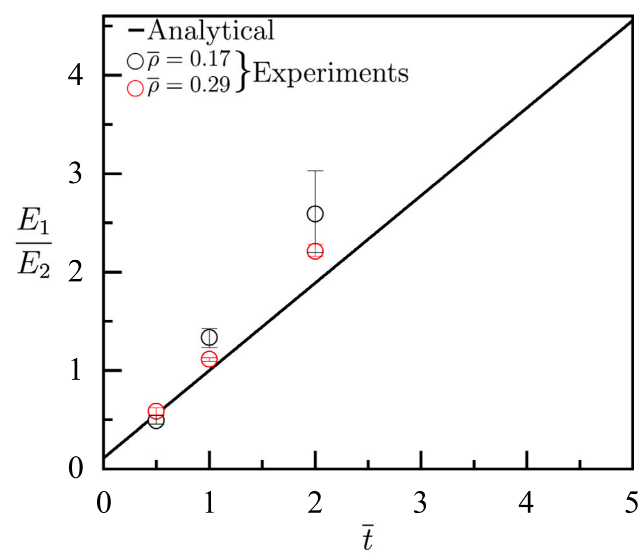

Fig. 15. Anisotropy ratio E_1/E_2 as a function of $\bar{t}$ for the triangular lattice. Experimental data points represent the average value of E_1 divided by the average value of E_2. For error bars, the upper limit is the maximum value of E_1 divided by the minimum value of E_2, whereas the lower limit is the minimum value of E_1 divided by the maximum value of E_2..

in which parameters s and c vary depending on the axial load P. When the bar is loaded in compression ($P > 0$), s and c are given by:

$$s = \frac{\lambda(\sin\lambda - \lambda\cos\lambda)}{2 - 2\cos\lambda - \lambda\sin\lambda}, \tag{A.3}$$

and

$$c = \frac{\lambda - \sin\lambda}{\sin\lambda - \lambda\cos\lambda}, \tag{A.4}$$

where

$$\lambda = \sqrt{\frac{P}{E_s I}}\,l. \tag{A.5}$$

Otherwise, when the bar is under tension ($P < 0$), s and c have the form:

$$s = s_1 = \frac{\lambda_1(\lambda_1\cosh\lambda_1 - \sinh\lambda_1)}{2 - 2\cosh\lambda_1 + \lambda_1\sinh\lambda_1}, \tag{A.6}$$

$$c = c_1 = \frac{\sinh\lambda_1 - \lambda_1}{\lambda_1\cosh\lambda_1 - \sinh\lambda_1}, \tag{A.7}$$

$$\lambda_1 = \sqrt{\frac{-P}{E_s I}}\,l, \tag{A.8}$$

where the subscript 1 is used simply to differentiate these expressions from those in (A.3)–(A.5). Finally, when the bar carries no axial load ($P = 0$), the parameters s and c are:

$$s = 4 \quad \text{and} \quad c = 0.5. \tag{A.9}$$

The approach to find the end constraint factor n is as follows. First, the periodic buckling shape with the longest wavelength is identified for each topology and for each loading direction. Then, equilibrium conditions and Eq. (A.1) are combined to form a constitutive equation from which λ can be solved. Once λ is known, it is straightforward to compute the end buckling constraint since $\lambda = \pi n$.

A.1. Triangular lattice

First, consider the triangular lattice compressed in the x_1 direction. For this scenario, Fan et al. [68] demonstrated that the periodic buckling shape illustrated in Fig. A.2a is the one associated with the lowest load. By equilibrium, the bending moment at joint a should be zero,

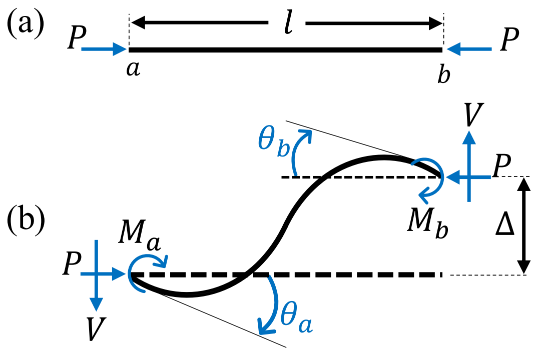

Fig. A.1. (a) A bar of length l subjected to a compressive load P. (b) The end rotations θ_a and θ_b generate bending moments M_a and M_b, respectively, and the transverse displacement Δ causes the shear force V.

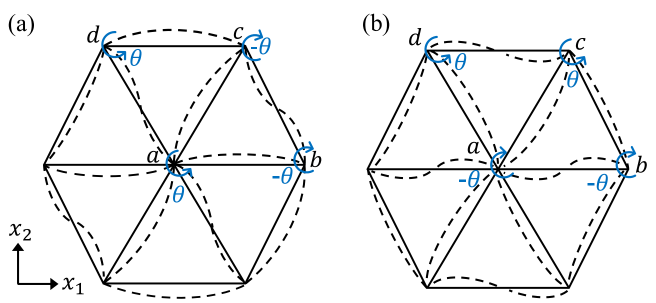

Fig. A.2. Periodic buckling shapes for a triangular lattice compressed in (a) x_1 and (b) x_2 directions.

and this can be expressed as:

$$M_{ab} + M_{ac} + M_{ad} = m_{ab}\theta + m_{ac}\theta + m_{ad}\theta = 0, \tag{A.10}$$

where the notation M_{ij} denotes the bending moment in bar ij at end i. The stiffness coefficients are obtained from Eq. (A.1) and are:

$$m_{ab} = \frac{2E_s I_{ab}}{l}(s - sc), \tag{A.11}$$

$$m_{ac} = \frac{2E_s I_{ac}}{l}(4 - 2), \tag{A.12}$$

$$m_{ad} = \frac{2E_s I_{ad}}{l}(4 + 2). \tag{A.13}$$

Note that m_{ab} includes parameters s and c since the bar is loaded in compression. In contrast, $s = 4$ and $c = 0.5$ for bars ac and ad since they carry no load, see Eq. (3). Here, the second moments of area are:

$$I_{ab} = \frac{bt_1{}^3}{12} \quad \text{and} \quad I_{ac} = I_{ad} = \frac{bt_2{}^3}{12}, \tag{A.14}$$

where b is the out-of-plane dimension. Substituting Eqs. (A.11)–(A.14) in (A.10) returns:

$$\bar{t}^{-3} \cdot \frac{\lambda(2\sin\lambda - \lambda\cos\lambda - \lambda)}{2 - 2\cos\lambda - \lambda\sin\lambda} + 8 = 0. \tag{A.15}$$

This equation was solved numerically and the end buckling constraint $n = \lambda/\pi$ is plotted as a function of $\bar{t}$ in Fig. A.3. The value of n decreases from 2 to 1 as $\bar{t}$ increases from 0 to 5. When the diagonal bars are significantly thicker than the horizontal bars, $\bar{t} \to 0$, the rotation θ, depicted in Fig. A.2a, is prevented and $n \to 2$. On the other hand, when the diagonal bars are markedly thinner than the horizontal bars, the nodes behave as pin joints and $n \to 1$.

Next, consider the triangular lattice loaded in compression along the x_2 direction. In this case, Fan et al. [68] showed that the lattice collapses according to the periodic buckling shape shown in Fig. A.2b.

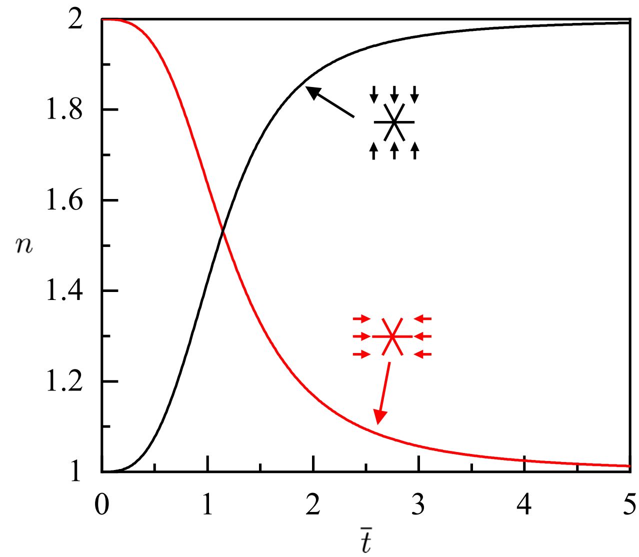

Fig. A.3. End constraint factor n as a function of $\bar{t} = t_1/t_2$ for a triangular lattice compressed in x_1 (red line) and x_2 (black line). (For interpretation of the references to colour in this figure legend, the reader is referred to the web version of this article.)

Again, the bending moment at joint a should be equal to zero; therefore Eq. (A.10) remains valid, but the stiffness coefficients become:

$$m_{ab} = \frac{2E_s I_{ab}}{l}(s_1 + s_1 c_1), \tag{A.16}$$

$$m_{ac} = \frac{2E_s I_{ac}}{l}(s - sc), \tag{A.17}$$

$$m_{ad} = \frac{2E_s I_{ad}}{l}(s - sc). \tag{A.18}$$

The parameters s and c now appear in m_{ac} and m_{ad} since the diagonal bars are in compression. In contrast, the horizontal bars are under tension, and consequently, the factors s_1 and c_1 appear in m_{ab}. In addition, $\lambda_1 = \lambda/\sqrt{2}$ since the magnitude of the axial force in the horizontal bars is half of that in the diagonal bars, see Eq. (10). Substituting Eqs. (A.16)–(A.18) in (A.10) returns:

$$\bar{t}^3 \cdot \frac{\lambda(\lambda\cosh(\lambda/\sqrt{2}) - 2\sqrt{2}\sinh(\lambda/\sqrt{2}) + \lambda)}{8 - 8\cosh(\lambda/\sqrt{2}) + 2\sqrt{2}\lambda\sinh(\lambda/\sqrt{2})} + \frac{\lambda(\sin\lambda - \lambda\cos\lambda)}{2 - 2\cos\lambda - \lambda\sin\lambda} = 0. \tag{A.19}$$

This equation was solved numerically and the end buckling constraint $n = \lambda/\pi$ is plotted as a function of $\bar{t}$ in Fig. A.3. Clearly, n increases from 1 to 2 as $\bar{t}$ increases from 0 to 5. For this loading scenario, the rotation θ, shown in Fig. A.2b, is prevented when the horizontal bars are significantly thicker than the diagonal bars.

A.2. Hexagonal lattice

When compressed in the x_1 direction, the hexagonal lattice buckles in a swaying mode as shown in Fig. A.4 [44]. Equilibrium dictates that the total bending moment and shear force at joint a should be zero. These two equilibrium equations are:

$$m_{ab}\theta + 2m_{ac}\theta + k_{ab}\Delta = 0, \tag{A.20}$$

$$2k_{ab}\theta + k^s_{ab}\Delta = 0, \tag{A.21}$$

where

$$m_{ab} = \frac{E_s I_{ab}}{l}(s + sc), \tag{A.22}$$

$$m_{ac} = \frac{E_s I_{ac}}{l}(4 - 2), \tag{A.23}$$

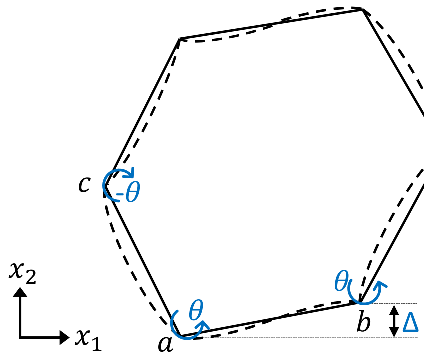

Fig. A.4. Periodic buckling shapes for a hexagonal lattice compressed in x_1 direction.

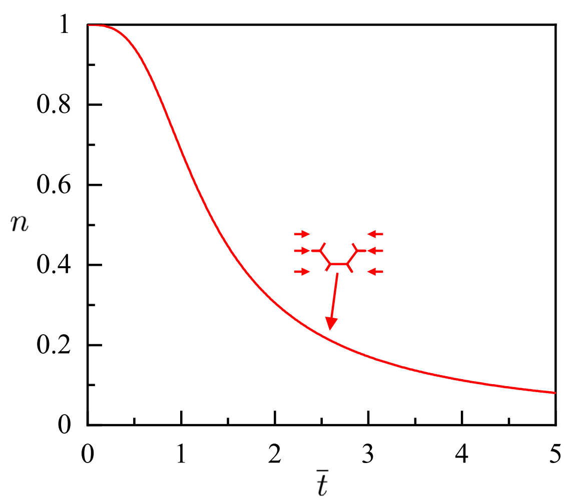

Fig. A.5. End constraint factor n as a function of $\bar{t} = t_1/t_2$ for a hexagonal lattice compressed in x_1 direction.

$$k_{ab} = \frac{E_s I_{ab}}{l^2}\bar{s}, \tag{A.24}$$

$$k^s_{ab} = \frac{E_s I_{ab}}{l^3}s^*. \tag{A.25}$$

Using Eq. (A.21), it is straightforward to express Δ as a function of θ and then substitute the result in Eq. (A.20). With the coefficients given in (A.22)–(A.25), and provided that $I_{ab}/I_{ac} = \bar{t}^3$, the governing equation becomes:

$$\bar{t}^3 \cdot \lambda(\cos\lambda - 1) + 4\sin\lambda = 0. \tag{A.26}$$

Solving this equation numerically returns the end constraint factor $n = \lambda/\pi$, which is plotted in Fig. A.5 as a function of $\bar{t}$. When $\bar{t} \to 0$, the horizontal bar behaves like a column clamped at both ends but free to translate in the transverse direction, and consequently, $n \to 1$. The rotation θ, shown in Fig. A.4, increases with increasing $\bar{t}$ and this leads to a reduction of the end constraint factor n. Finally, note that when $\bar{t} = 1$ we find $n = 0.686$, which is the same value obtained by Gibson and Ashby [44].

Appendix B. Supplementary data

Supplementary material related to this article can be found online at https://doi.org/10.1016/j.ijmecsci.2022.107079.

References

[1] Ashby MF. Hybrid materials to expand the boundaries of material-property space. J Am Ceram Soc 2011;94:s3–14.

[2] Montemayor L, Chernow V, Greer JR. Materials by design: Using architecture in material design to reach new property spaces. MRS Bull 2015;40(12):1122–9.

[3] Ashby MF. The properties of foams and lattices. Philos Trans R Soc A 2006;364(1838):15–30.

[4] Fleck NA, Deshpande VS, Ashby MF. Micro-architectured materials: past, present and future. Proc R Soc Lond Ser A Math Phys Eng Sci 2010;466(2121):2495–516.

[5] Berger JB, Wadley HNG, McMeeking RM. Mechanical metamaterials at the theoretical limit of isotropic elastic stiffness. Nature 2017;543(7646):533–7.

[6] Hsieh M-T, Endo B, Zhang Y, Bauer J, Valdevit L. The mechanical response of cellular materials with spinodal topologies. J Mech Phys Solids 2019;125:401–19.

[7] Tancogne-Dejean T, Diamantopoulou M, Gorji MB, Bonatti C, Mohr D. Metamaterials: 3D plate-lattices: An emerging class of low-density metamaterial exhibiting optimal isotropic stiffness. Adv Mater 2018;30(45):1870337.

[8] Maconachie T, Leary M, Lozanovski B, Zhang X, Qian M, Faruque O, Brandt M. SLM Lattice structures: properties, performance, applications and challenges. Mater Des 2019;183:108137.

[9] Schaedler TA, Carter WB. Architected cellular materials. Annu Rev Mater Res 2016;46(1):187–210.

[10] Gümrük R, Mines RAW. Compressive behaviour of stainless steel micro-lattice structures. Int J Mech Sci 2013;68:125–39.

[11] Liu L, Kamm P, Garcia-Moreno F, Banhart J, Pasini D. Elastic and failure response of imperfect three-dimensional metallic lattices: the role of geometric defects induced by selective laser melting. J Mech Phys Solids 2017;107:160–84.

[12] Tancogne-Dejean T, Spierings AB, Mohr D. Additively-manufactured metallic micro-lattice materials for high specific energy absorption under static and dynamic loading. Acta Mater 2016;116:14–28.

[13] Yan C, Hao L, Hussein A, Young P, Raymont D. Advanced lightweight 316l stainless steel cellular lattice structures fabricated via selective laser melting. Mater Des 2014;55:533–41.

[14] Zhou H, Cao X, Li C, Zhang X, Fan H, Lei H, Fang D. Design of self-supporting lattices for additive manufacturing. J Mech Phys Solids 2021;148:104298.

[15] Bonatti C, Mohr D. Mechanical performance of additively-manufactured anisotropic and isotropic smooth shell-lattice materials: simulations & experiments. J Mech Phys Solids 2019;122:1–26.

[16] Bonatti C, Mohr D. Smooth-shell metamaterials of cubic symmetry: Anisotropic elasticity, yield strength and specific energy absorption. Acta Mater 2019;164:301–21.

[17] Lv W, Li D, Dong L. Study on mechanical properties of a hierarchical octet-truss structure. Compos Struct 2020;249:112640.

[18] Muth JT, Dixon PG, Woish L, Gibson LJ, Lewis JA. Architected cellular ceramics with tailored stiffness via direct foam writing. Proc Natl Acad Sci USA 2017;114(8):1832–7.

[19] Rayneau-Kirkhope D, Mao Y, Farr R, Segal J. Hierarchical space frames for high mechanical efficiency: Fabrication and mechanical testing. Mech Res Commun 2012;46:41–6.

[20] Sha Y, Jiani L, Haoyu C, Ritchie RO, Jun X. Design and strengthening mechanisms in hierarchical architected materials processed using additive manufacturing. Int J Mech Sci 2018;149:150–63.

[21] Yin S, Chen H, Li J, Yu TX, Xu J. Effects of architecture level on mechanical properties of hierarchical lattice materials. Int J Mech Sci 2019;157–158(37):282–92.

[22] Zhang W, Yin S, Yu T, Xu J. Crushing resistance and energy absorption of pomelo peel inspired hierarchical honeycomb. Int J Impact Eng 2019;125:163–72.

[23] Bauer J, Schroer A, Schwaiger R, Kraft O. Approaching theoretical strength in glassy carbon nanolattices. Nat Mat 2016;15(4):438–43.

[24] Bauer J, Meza LR, Schaedler TA, Schwaiger R, Zheng X, Valdevit L. Nanolattices: an emerging class of mechanical metamaterials. Adv Mater 2017;29(40):1701850.

[25] Meza LR, Das S, Greer JR. Strong, lightweight, and recoverable three-dimensional ceramic nanolattices. Science 2014;345(6202):1322–6.

[26] Meza LR, Phlipot GP, Portela CM, Maggi A, Montemayor LC, Comella A, Kochmann DM, Greer JR. Reexamining the mechanical property space of three-dimensional lattice architectures. Acta Mater 2017;140:424–32.

[27] Schaedler TA, Jacobsen AJ, Torrents A, Sorensen AE, Lian J, Greer JR, Valdevit L, Carter WB. Ultralight metallic microlattices. Science 2011;334(6058):962–5.

[28] Cao X, Duan S, Liang J, Wen W, Fang D. Mechanical properties of an improved 3D-printed rhombic dodecahedron stainless steel lattice structure of variable cross section. Int J Mech Sci 2018;145:53–63.

[29] Qi D, Yu H, Liu M, Huang H, Xu S, Xia Y, Qian G, Wu W. Mechanical behaviors of SLM additive manufactured octet-truss and truncated-octahedron lattice structures with uniform and taper beams. Int J Mech Sci 2019;163:105091.

[30] Tancogne-Dejean T, Mohr D. Stiffness and specific energy absorption of additively-manufactured metallic BCC metamaterials composed of tapered beams. Int J Mech Sci 2018;141:101–16.

[31] Harris JA, McShane GJ. Metallic stacked origami cellular materials: additive manufacturing, properties, and modelling. Int J Solids Struct 2020;185–186:448–66.

[32] Ruschel AL, Zok FW. A bi-material concept for periodic dissipative lattices. J Mech Phys Solids 2020;145:104144.

[33] Li K, Seiler PE, Deshpande VS, Fleck NA. Regulation of notch sensitivity of lattice materials by strut topology. Int J Mech Sci 2021;192:106137.
[34] Seiler PE, Li K, Deshpande VS, Fleck NA. The influence of strut waviness on the tensile response of lattice materials. J Appl Mech 2021;88(3):1–11.
[35] Khanoki SA, Pasini D. Multiscale design and multiobjective optimization of orthopedic hip implants with functionally graded cellular material. J Biomech Eng 2012;134:031004.
[36] Maskery I, Aboulkhair NT, Aremu AO, Tuck CJ, Ashcroft IA, Wildman RD, Hague RJM. A mechanical property evaluation of graded density Al-Si10-Mg lattice structures manufactured by selective laser melting. Mater Sci Eng A 2016;670:264–74.
[37] Niknam H, Akbarzadeh AH. Graded lattice structures: Simultaneous enhancement in stiffness and energy absorption. Mater Des 2020;196:109129.
[38] Wang Y, Zhang L, Daynes S, Zhang H, Feih S, Wang MY. Design of graded lattice structure with optimized mesostructures for additive manufacturing. Mater Des 2018;142:114–23.
[39] Yang C, Li QM, Wang Y. Compressive properties of cuttlebone-like lattice (CLL) materials with functionally graded density. Eur J Mech A Solids 2021;87:104215.
[40] Challis VJ, Roberts AP, Wilkins AH. Design of three dimensional isotropic microstructures for maximized stiffness and conductivity. Int J Solids Struct 2008;45(14):4130–46.
[41] Kollmann HT, Abueidda DW, Koric S, Guleryuz E, Sobh NA. Deep learning for topology optimization of 2D metamaterials. Mater Des 2020;196:109098.
[42] Osanov M, Guest JK. Topology optimization for architected materials design. Annu Rev Mater Res 2016;46(1):211–33.
[43] Sigmund O. Materials with prescribed constitutive parameters: an inverse homogenization problem. Int J Solids Struct 1994;31(17):2313–29.
[44] Gibson LJ, Ashby MF. Cellular Solids: Structure And Properties. 2nd edition. Cambridge University Press; 1997.
[45] Wang A-J, McDowell DL. In-plane stiffness and yield strength of periodic metal honeycombs. J Eng Mater Technol 2004;126(2):137–56.
[46] Gu H, Pavier M, Shterenlikht A. Experimental study of modulus, strength and toughness of 2D triangular lattices. Int J Solids Struct 2018;152–153:207–16.
[47] Klintworth JW, Stronge WJ. Elasto-plastic yield limits and deformation laws for transversely crushed honeycombs. Int J Mech Sci 1988;30(3):273–92.
[48] Zhang J, Ashby MF. Buckling of honeycombs under in-plane biaxial stresses. Int J Mech Sci 1992;34(6):491–509.
[49] Papka SD, Kyriakides S. In-plane compressive response and crushing of honeycomb. J Mech Phys Solids 1994;42(10):1499–532.
[50] Papka SD, Kyriakides S. Experiments and full-scale numerical simulations of in-plane crushing of a honeycomb. Acta Mater 1998;46(8):2765–76.
[51] Wilbert A, Jang W-Y, Kyriakides S, Floccari JF. Buckling and progressive crushing of laterally loaded honeycomb. Int J Solids Struct 2011;48(5):803–16.
[52] Asprone D, Auricchio F, Menna C, Morganti S, Prota A, Reali A. Statistical finite element analysis of the buckling behavior of honeycomb structures. Compos Struct 2013;105:240–55.
[53] Cricrì G, Perrella M, Calì C. Honeycomb failure processes under in-plane loading. Composites B 2013;45(1):1079–90.
[54] Jang W-Y, Kyriakides S. On the buckling and crushing of expanded honeycomb. Int J Mech Sci 2015;91:81–90.
[55] Simone AE, Gibson LJ. Effects of solid distribution on the stiffness and strength of metallic foams. Acta Mater 1998;46(6):2139–50.
[56] Chuang C-H, Huang J-S. Elastic moduli and plastic collapse strength of hexagonal honeycombs with plateau borders. Int J Mech Sci 2002;44(9):1827–44.
[57] Chuang C-H, Huang J-S. Theoretical expressions for describing the stiffness and strength of regular hexagonal honeycombs with plateau borders. Mater Des 2003;24(4):263–72.
[58] Zhu HX, Chen CY. Combined effects of relative density and material distribution on the mechanical properties of metallic honeycombs. Mech Mater 2011;43(5):276–86.
[59] Lira C, Scarpa F. Transverse shear stiffness of thickness gradient honeycombs. Compos Sci Tech 2010;70(6):930–6.
[60] Sun G, Jiang H, Fang J, Li G, Li Q. Crashworthiness of vertex based hierarchical honeycombs in out-of-plane impact. Mater Des 2016;110:705–19.
[61] Tao Y, Duan S, Wen W, Pei Y, Fang D. Enhanced out-of-plane crushing strength and energy absorption of in-plane graded honeycombs. Compos B: Eng 2017;118:33–40.
[62] Duan S, Tao Y, Lei H, Wen W, Liang J, Fang D. Enhanced out-of-plane compressive strength and energy absorption of 3D printed square and hexagonal honeycombs with variable-thickness cell edges. Extreme Mech Lett 2018;18:9–18.
[63] Xu F, Zhang X, Zhang H. A review on functionally graded structures and materials for energy absorption. Eng Struct 2018;171:309–25.
[64] Wu Y, Sun L, Yang P, Fang J, Li W. Energy absorption of additively manufactured functionally bi-graded thickness honeycombs subjected to axial loads. Thin-Walled Struct 2021;164:107810.
[65] Qi C, Jiang F, Yang S. Advanced honeycomb designs for improving mechanical properties: A review. Compos B: Eng 2021;227:109393.
[66] Timoshenko S, Gere JM. Theory Of Elasticity Stability. New York: McGraw-Hill; 1961.
[67] Bažant ZP, Cedolin L. Stability Of Structures: Elastic, Inelastic, Fracture And Damage Theories. New York: Oxford University Press; 1991.
[68] Fan H, Jin F, Fang D. Uniaxial local buckling strength of periodic lattice composites. Mater Des 2009;30(10):4136–45.
[69] Drago A, Pindera M-J. Micro-macromechanical analysis of heterogeneous materials: Macroscopically homogeneous vs periodic microstructures. Compos Sci Technol 2007;67(6):1243–63.
[70] Tankasala HC, Deshpande VS, Fleck NA. Tensile response of elastoplastic lattices at finite strain. J Mech Phys Solids 2017;109:307–30.
[71] Onck PR, Andrews EW, Gibson LJ. Size effects in ductile cellular solids. Part I: modeling. Int J Mech Sci 2001;43(3):681–99.
[72] Zener C. Contributions to the theory of beta-phase alloys. Phys Rev 1947;71:846–51.
[73] Zhu HX, Mills NJ. The in-plane non-linear compression of regular honeycombs. Int J Solids Struct 2000;37(13):1931–49.
[74] Chuang C-H, Huang J-S. Effects of solid distribution on the elastic buckling of honeycombs. Int J Mech Sci 2002;44(7):1429–43.
[75] Yang M-Y, Huang J-S, Hu J-W. Elastic buckling of hexagonal honeycombs with dual imperfections. Compos Struct 2008;82(3):326–35.
[76] Triantafyllidis N, Schraad MW. Onset of failure in aluminum honeycombs under general in-plane loading. J Mech Phys Solids 1998;46(6):1089–124.
[77] Ohno N, Okumura D, Noguchi H. Microscopic symmetric bifurcation condition of cellular solids based on a homogenization theory of finite deformation. J Mech Phys Solids 2002;50(5):1125–53.
[78] Okumura D, Ohno N, Noguchi H. Post-buckling analysis of elastic honeycombs subject to in-plane biaxial compression. Int J Solids Struct 2002;39(13):3487–503.
[79] Okumura D, Ohno N, Noguchi H. Elastoplastic microscopic bifurcation and post-bifurcation behavior of periodic cellular solids. J Mech Phys Solids 2004;52(3):641–66.
[80] Yang M-Y, Huang J-S. Elastic buckling of regular hexagonal honeycombs with plateau borders under biaxial compression. Compos Struct 2005;71(2):229–37.